

A wide-field photometric survey for extratidal tails around five metal-poor globular clusters in the Galactic halo ¹

Sang-Hyun Chun², Jae-Woo Kim³, Sangmo T. Sohn^{4,7}, Jang-Hyun Park⁵, Wonyong Han⁵,
Ho-Il Kim⁵, Young-Wook Lee^{2,4}, Myung Gyoon Lee⁶, Sang-Gak Lee⁶, and Young-Jong
Sohn²

Received _____; accepted _____

To be submitted to the *Astronomical Journal*

²Department of Astronomy, Yonsei University, Seoul 120-749, Korea, sohnyj@yonsei.ac.kr

³Institute for Computational Cosmology, Department of Physics, Durham University, South Road, Durham DH1 3LE, UK

⁴Center for Space Astrophysics, Yonsei University, Seoul 120-749, Korea

⁵Korea Astronomy and Space Science Institute, Daejeon 305-348, Korea

⁶Astronomy Program Department of Physics and Astronomy, Seoul National University, Seoul 151-742, Korea

⁷Current address: Space Telescope Science Institute, 3700 San Martin Drive, Baltimore, MD 21218

ABSTRACT

Wide-field deep $g'r'i'$ images obtained with the Megacam of the Canada-France-Hawaii Telescope (CFHT) are used to investigate the spatial configuration of stars around five metal-poor globular clusters M15, M30, M53, NGC 5053, and NGC 5466, in a field-of-view $\sim 3^\circ$. Applying a mask filtering algorithm to the color-magnitude diagrams of the observed stars, we sorted cluster's member star candidates that are used to examine the characteristics of the spatial stellar distribution surrounding the target clusters. The smoothed surface density maps and the overlaid isodensity contours indicate that all of the five metal-poor globular clusters exhibit strong evidence of extratidal overdensity features over their tidal radii, in the form of extended tidal tails around the clusters. The orientations of the observed extratidal features show signatures of tidal tails tracing the clusters' orbits, inferred from their proper motions, and effects of dynamical interactions with the Galaxy. Our findings include detections of a tidal bridge-like feature and an envelope structure around the pair of globular clusters M53 and NGC 5053. The observed radial surface density profiles of target clusters have a deviation from theoretical King models, for which the profiles show a break at $0.5 \sim 0.7r_t$, extending the overdensity features out to $1.5 \sim 2r_t$. Both radial surface density profiles for different angular sections and azimuthal number density profiles confirm the overdensity features of tidal tails around the five metal-poor globular clusters. Our results add further observational evidence that the observed metal-poor halo globular clusters originate from an accreted satellite system, indicative of the merging scenario of the formation of the Galactic halo.

Subject headings: Galaxy: halo — Galaxy: structure — globular clusters: general —

globular clusters: individual(M15, M30, M53, NGC 5053, NGC 5466)

1. INTRODUCTION

In the current cold dark matter cosmology, the favorably accepted galaxy formation paradigm is that galaxies like the Milky Way were assembled from a series of accretion events involving lower mass subunits, in a fashion similar to galaxy cluster formation (White & Rees 1978; Blumentahl et al. 1984; Davis et al. 1985; Tormen 1997, 1998; Ghigna et al. 1998; Tormen et al. 1998; Ghigna et al. 2000). If these favored hierarchical models are correct, then the stellar halo of the Galaxy should form through tidal disruption and accretion of numerous low-mass fragments such as dwarf satellite galaxies (e.g., Johnston 1998; Klypin et al. 1999; Moore et al. 1999, 2006; Bullock et al. 2001; Bullock & Johnston 2005; Abadi et al. 2006). These merging events may leave traces of large-scale stellar substructures in the outer Galactic halo, and remnant stellar systems of the parent fragments with a long dynamical disruption time scale.

Since the classical Searle & Zinn (1978) scenario of the formation of the Galaxy was first suggested, there has been more observational evidence to support the accretion scenario that the halo population of the Milky Way and globular clusters originated through the gradual merging and disruption of fragments. This evidence includes (1) a large-scale stellar substructure through the Galactic halo, (2) a feature of multiple populations in a globular cluster that is indicative of the remnant nuclei of a merged dwarf spheroidal galaxy, (3) an extended tidal feature in a spatial stellar density distribution, such as tidal tails and halos around a globular cluster, which might trace the cluster’s orbit, and (4) a spatially aligned configuration of a group of several globular clusters. Consequently, globular clusters in the

¹Based on observations carried out at the Canada-France-Hawaii Telescope, operated by the National Research Council of Canada, the Centre National de la Recherche Scientifique de France, and the University of Hawaii. This is part of the Searching for the Galactic Halo project using the CFHT, organized by the Korea Astronomy and Space Science Institute.

Galactic halo and their surroundings, as the local manifestations of the hierarchical Galaxy formation, are the best places to look for the substructure of stellar distribution in the Galactic outer halo.

For the first note of large-scale stellar substructures through the Galactic halo, Lynden-Bell (1982) indicated that several dwarf spheroidal galaxies and outer halo clusters lie near two great circles passing close to the Galactic poles, i.e., the Magellanic stream and the Fornax-Leo-Sculptor stream. The spatially associated distribution of dwarf galaxies is interpreted as a result of the accretion of parent satellite galaxies which are considered the external fragments. Furthermore, recent large-scale surveys have uncovered several complex substructures of the stellar Galactic halo (e.g., Yanny et al. 2000, 2003; Ivezić et al. 2000; Newberg et al. 2002, 2009; Martin et al. 2004; Rocha-Pinto et al. 2004; Martinez-Delgado et al. 2005; Grillmair & Dionatos 2006; Belokurov et al. 2006a; Jurić et al. 2008). The most striking example in this category is the discovery of the trails of stellar debris associated with the Sagittarius dwarf galaxy (Ibata et al. 1994, 1995, 1997, 2001a; Majewski et al. 2003; Newberg et al. 2003).

Stellar population studies of globular clusters have suggested that the brightest globular clusters in the Galaxy are actually the remnant nuclei of dwarf spheroidal galaxies. Indeed, Lee et al. (1999) detected multiple stellar populations of different age and metallicity in ω Centauri, the most massive globular cluster in the Galaxy. This is reminiscent of the Sagittarius dwarf galaxy, which includes M54 as its nucleus, the second most massive globular cluster in the Galaxy. Extending previous suggestions, van den Bergh (2000) suggested that the majority of metal-poor young globular clusters in the outer halo originated from dwarf spheroidal galaxies, and it would be worthwhile to find their parent galaxies. Recently, Lee et al. (2007) found that globular clusters with an extended horizontal-branch (EHB) would be kinematically decoupled from the normal clusters, and,

that these are the relics of the first building blocks of the Galaxy formation.

If present Galactic globular clusters formed within larger stellar systems, they are likely surrounded by extratidal halos and tails made up of stars that were tidally stripped from their parent systems. Also, they would have lost the majority fraction of the initial mass due to their internal and external dynamical effects, such as tidal heating and stripping (Ostriker et al. 1972; Aguilar et al. 1988; Kundic & Ostriker 1995; Gnedin & Ostriker 1997; Murali & Weinberg 1997; Gnedin et al. 1999; Baumgardt & Makino 2003). This information suggests that surroundings around globular clusters provide an excellent example of such a structure, and as a result we might expect to figure out them by wide-field deep photometry (e.g., Martinez-Delgado et al. 2004). In the first attempt to find such a tidal feature around globular clusters, Grillmair et al. (1995) examined the stellar density distribution around 12 globular clusters and found that many globular clusters have surface density profiles significantly exceeding the prediction of formal King models and also extending outside the tidal radius by extratidal stars. Until now, signatures of the extratidal overdensity feature have been found in over 30 globular clusters both in the Galaxy and in M31 (Grillmair et al. 1996; Lehmann & Scholz 1997; Leon et al. 2000; Testa et al. 2000; Siegel et al. 2001; Lee et al. 2003; Sohn et al. 2003; Lauchner et al. 2006). Recent star count surveys have revealed tidal structures stretching many degrees beyond the cluster tidal radius, for which the most spectacular examples include Palomar 5 (Odenkirchen et al. 2001, 2003, 2009; Rockosi et al. 2002; Grillmair & Dionatos 2006) and NGC 5466 (Belokurov et al. 2006b; Grillmair & Johnson 2006) with tails extending as much as 22° and 45° , respectively. As a consequence of these previous studies, it has been apparent that tidal tails of globular clusters are likely aligned with the cluster's orbit because the debris produced by a dissolving globular cluster will have similar orbital parameters as the cluster itself. Recently, Odenkirchen et al. (2009) presented kinematics of debris around Palomar 5 to suggest that the cluster's orbit in the sky is not exactly

aligned with its tidal tails. Here, we also note that Koch et al. (2004) found that the luminosity function (LF) in the tails of Palomar 5 agrees well with the LF in the outer region of the cluster but differs from the LF in the cluster’s core. On the theoretical side, many numerical simulations have reproduced a structure of tidal tails around globular clusters (Dehnen et al. 2004; di Matteo et al. 2005; Lee et al. 2006; Fellhauer et al. 2007; Kupper et al. 2008). Indeed, the cluster-galaxy interaction can cause stars to escape the cluster’s gravitational potential, and then the unbounded stars remain in the vicinity of the cluster for several orbital periods to become tidal debris-forming tails in front of and behind the cluster’s orbit (Combes et al. 1999; Yim & Lee 2002; Capuzzo Dolcetta et al. 2005; Montouri et al. 2007).

The spatial alignment of the globular cluster system might also play an important role in untangling the possibility that the Galactic halo may have formed from the accretion of dwarf galaxies. For a statistically significant instance, the Sagittarius dwarf spheroidal has its own globular cluster system associated with several halo clusters beyond a galactocentric distance $R_{GC} \geq 10$ kpc (Bellazzini et al. 2003; Tautvaišienė et al. 2004; Sbordone et al. 2005). This attests to the fact that even minor mergers play a key role in the formation and structure of the Galaxy. Furthermore, Yoon & Lee (2002) found that a group of the seven lowest metallicity ($[\text{Fe}/\text{H}] < -2.0$) clusters (i.e., NGC 5053, NGC 5466, M15, M30, M53, M68, and M92, classified as Oosterhoff group II-b) displays a planer alignment in the outer halo perpendicular to the line joining the present position of the Sun and the Galactic center. They also suggested that these metal-poor clusters were originally born in the Large Magellanic Cloud (LMC) and have recently been captured by the Galaxy through the Magellanic plane. Indeed, the configuration of the Milky Way with the stream of clusters and satellites in the Magellanic plane closely resembles the stellar stream in the halo of M31, which lies along the satellites M32 and NGC 205 (Ibata et al. 2001b). Of the seven low-metallicity clusters in the Magellanic plane (Yoon & Lee 2002), NGC 5466 has been

the subject of extensive investigations from wide-field photometric analyses of the SDSS data (Belokurov et al. 2006b; Grillmair & Johnson 2006) to show a feature of extended extratidal tails outside the tidal radius along the cluster’s orbit. The other clusters in the Magellanic plane have not yet shown any strong observational evidences of extratidal tails along the clusters’ orbits. Instead, hints of a weak evidence of extratidal halo structure outside the tidal radius have been reported for three clusters, i.e., M15 (Grillmair et al. 1995), M68 (Grillmair et al. 1995), and M92 (Testa et al. 2000; Lee et al. 2003).

In this paper, we investigate the two-dimensional distribution of stars around five clusters (M15, M30, M53, NGC 5053, and NGC 5466) of the seven extreme metal-poor globular clusters of the Oosterhoof group II-b (Yoon & Lee 2002) and we report the spatial structure of the stellar distribution in the vicinity of the clusters. Wide-field $g'r'i'$ imaging photometric data for the five globular clusters have been secured from the observations of the Megacam attached to the Canada-France-Hawaii Telescope (CFHT). Table 1 contains basic data for the five target globular clusters. Note that the other two low-metallicity clusters M68 and M92 have not been observed at the present observing runs. Section 2 presents the observations, data reduction procedure, and photometric measurements of the resolved stars. The statistical mask filtering method for the photometric selection of clusters’ member stars is presented in Section 3. In Section 4, we investigate extratidal features around the target clusters by using two-dimensional stellar density maps, radial surface density profiles, and azimuthal number density profiles. The results are discussed and summarized in Section 5.

2. OBSERVATIONS AND DATA REDUCTION

The wide-field photometric imaging data for M15, M30, M53, NGC 5053, and NGC 5466 were taken in Queued Service Observing (QSO) of the 3.6 m CFHT. The detector in

the Megacam is a mosaic of thirty-six 2048×4612 pixels² CCDs, that together cover an area of $\sim 1^\circ \times 1^\circ$ wide-field-of-view with a plate scale of $0.187''$ pixel⁻¹. We covered nine and eight Megacam observing fields for the surroundings of two clusters, M15 and NGC 5466, and of one cluster, M30, respectively. For each cluster, one field was centered to imbed the cluster itself, while the other fields outside the object were chosen so as to cover a total field of view of $\sim 3^\circ \times 3^\circ$. Since the tidal radii of the clusters are in the range of $14' \sim 22'$, a set of these observations provided sufficiently large spatial coverage for our purpose of studying the stellar density distribution and tidal features in the vicinity of the globular clusters. The other two clusters, M53 and NGC 5053, compose a close neighbor pairing system with an angular separation of $\sim 1^\circ$ on the sky, and the two clusters have nearly the same distance modulus. Note that the close proximity of the two clusters is very unusual in the outer halo of the Galaxy. In order to search for direct observational evidence of a tidal interaction between the two clusters and tidal features around each cluster, we observed nine Megacam fields in a pattern as shown in Figure 1, covering both of the clusters.

The imaging data for the target clusters were taken in three SDSS filters, g' , r' , and i' , respectively. Single exposures were taken for each filter without a dither pattern. The exposure times to be used were determined so as to achieve a limiting magnitude of ~ 3 magnitudes below the main sequence turnoff of each cluster, i.e., $g' \sim 23$ mag. Table 2 presents the journal of the observations. Stars have $0.6 - 1.0$ arcsec FWHM in the final processed images, depending on the filter.

The removal of instrumental signatures from the raw images was done with the ELIXIR processing pipeline at the CFHT (Magnier & Cuillandre 2004). This processing includes bias subtraction, flat fielding, and the subtraction of a fringe frame. Also, the pre-analysis of the ELIXIR produced 36 CCD images of a given mosaic with the same zeropoint and magnitude scale. A typical value of the residuals across a mosaic is ~ 0.0086 mag.

The photometric measurements were made with the point-spread-function (PSF) fitting programs DAOPHOT II and ALLSTAR (Stetson 1987; Stetson & Harris 1988). Analysis was done on a single-chip basis for all exposures of the 36 CCD chips on the mosaic. A PSF varying quadratically through positions was constructed using $\sim 100 - 200$ bright and isolated stars for a heavily crowded image and $\sim 25 - 50$ stars for a less crowded image. The quality of each PSF has been improved by removing neighboring stars around selected PSF stars and reconstructing the PSF iteratively. Instrumental magnitudes for each star based on the determined PSF were then measured by the ALLSTAR process. Aperture correction was applied by using the growth-curve analysis package DAOGROW (Stetson & Harris 1988; Stetson 1990) to compensate for the missing light lying outside of the PSF tail for every star in each frame. After the aperture correction, DAOMATCH and DAOMASTER (Stetson 1992) were used to match stars on each CCD chip, and coordinate offsets for each field were estimated from the positional data in each frame. We then converted all the positional data of each chip on a mosaic into a single coordinate system. Finally, the positional data for stars in the observed Megacam fields were transformed into the equatorial coordinate system, by using the USNO-B catalog (Monet et al. 2003) for bright stars in the fields.

The measured instrumental magnitudes were photometrically calibrated using the zeropoints that were computed from standard star observations during each Megacam run. The calibrated magnitudes were finally converted into a standard SDSS photometric system, as defined by Smith et al. (2002). Individual stars with poorly determined photometric measurements, as reported by ALLSTAR, were removed to limit the number of spurious detections for each cluster. Objects with χ and SHARP values that markedly deviated from the values for the majority of objects were rejected, and this removed objects near the faint limit of the data and extended objects such as faint galaxies. In order to correct the interstellar extinction, we derived the individual extinction value for each detected star

from the maps of Schlegel et al. (1998), and these values have been subtracted from the observed magnitude. Finally a total of 239 600, 100 069, and 69 901 stars were detected for each $\sim 3^\circ \times 3^\circ$ field of clusters M15, M30, and NGC 5466, respectively. For nine Megacam fields of M53 and NGC 5053, we detected 79 075 stars in all three $g'r'i'$ images.

3. PHOTOMETRIC SELECTION OF THE CLUSTER STARS

A feature of spatial stellar distribution around globular clusters represents the sum of the unbound stars released by the cluster and the field stars. Therefore, to trace the overdensity features around the clusters in detail, one needs to minimize the number of contaminating field stars in a given sample and to enhance the contrast between the cluster and the field. In the first statistical attempt to discriminate field stars, Grillmair et al. (1995) introduced a polygonal mask method in a color-magnitude (C-M) space in which only field stars with colors and magnitudes that resemble those of cluster stars are counted to optimize the ratio of the cluster stars to field stars. However, the defined mask in a C-M space does not provide the optimal method to map the spatial stellar distribution around sparsely populated globular clusters because many bins with a small number of stars in a C-M space can be statistically excluded from the mask. To reduce the disadvantage of poor statistics, Odenkirchen et al. (2001) introduced a new method to compress the photometric data in a C-M space by constructing new color indices from which the weighted sum of field stars plus cluster stars yields the best approximation of the observed total C-M distribution. In the present study, we have applied the same method of Odenkirchen et al. (2001) to define a C-M mask with new color indices c_1 and c_2 and $g'r'i'$ magnitudes for detected stars in the vicinity of each cluster.

First, we defined two orthogonal color indices c_1 and c_2 from a linear distribution of stars in a $(g' - r', r' - i')$ color-color diagram. Indeed, the choice of the indices is such

that the main axis of the almost one-dimensional locus of cluster stars in the color-color plane lies along the c_1 axis, while the c_2 axis is perpendicular to it (e.g., Odenkirchen et al. 2001, 2003). Equation (1) presents general forms of the rotational transformation of the $(g' - r', r' - i')$ plane to the coordinate system of (c_1, c_2) . Here, the systematic variation of color with magnitude is mostly contained in c_1 , while variations in c_2 are mostly due to the observational photometric errors, as noted in Odenkirchen et al. (2001). Transformation coefficients a and b for each cluster were determined by using the least-squared fit to the data, which are listed in Table 3. Assuming that two clusters M53 and NGC 5053 have very similar color-magnitude diagrams (CMDs) with almost identical metallicity and age (e.g., Heasley & Christian 1991; Rey et al. 1998), and nearly the same distance modulus, we estimated a set of c_1, c_2 and a, b for all stars detected in both of the clusters.

$$\begin{aligned} c_1 &= a(g' - r') + b(r' - i'), \\ c_2 &= -b(g' - r') + a(r' - i') \end{aligned} \tag{1}$$

In (c_2, i') space of stars located in the central region of the clusters, we preselected the sample in c_2 by discarding all stars with $|c_2| > 2\sigma_{c_2}(i')$, where $\sigma_{c_2}(i')$ is the photometric errors in c_2 for stars with magnitude i' . The radii of the cluster's central regions were empirically defined in the unit of half-mass radius (r_h) or core radius (r_c) of the cluster in order to find appropriate color-magnitude sequences of stars in each cluster. The heavy lines in the leftmost panels in Figure 2 give $2\sigma_{c_2}(i')$ limits for stars in each cluster. For a system of M53 and NGC 5053, we selected a central region of the clusters as the sum of $3r_h < r \leq 8r_h$ for M53 and $r_c < r \leq 4r_c$ for NGC 5053.

For stars preselected in the (c_2, i') plane, we then applied the C-M mask filtering method (Grillmair et al. 1995) in the (c_1, i') plane, from which we eventually extracted a sample of stars to trace their spatial configuration around the clusters. We first examined

the distribution of the cluster population in the (c_1, i') space by means of preselected stars in the cluster central area and the background field areas. The cluster central area was assigned so as to have the largest number ratio of stars enclosed $2\sigma_{c_1}(i')$ and those outside $2\sigma_{c_1}(i')$ in the (c_1, i') plane for all preselected stars within the radius of the circle. Here, $\sigma_{c_1}(i')$ is an estimated standard deviation of i' magnitudes of stars at c_1 . The second from the left panels in Figure 2 show (c_1, i') CMDs of stars within the radii of the determined central areas of the clusters, which are denoted by circles centered on each cluster in Figure 3. We also selected four background field areas in circles at sufficiently distant parts from the cluster. For three isolated target clusters, M15, M30, and NGC 5466, the sum of the background field areas is nine times those of the determined cluster's area, as shown in Figure 3. Note that, as shown in the bottom-right panel of Figure 3, the background areas for a field of M53 and NGC 5053 were empirically selected to have a total area five times larger than the sum of central areas of the two clusters. The third and fourth panels of Figure 2, from left to right, show the (c_1, i') CMDs of the stars in the selective background regions and in the total survey region for each cluster, respectively.

Next, we compared the (c_1, i') CMD of stars in the selective cluster central region with that of stars in the assigned background regions, from which we select areas in the (c_1, i') plane with high significance about the expected true number of cluster stars. This procedure was done by subdividing the C-M plane into small subgrid elements with a 0.025-mag width in c_1 and a 0.12-mag height in i' . Then, we measured the number of stars in each subgrid element of cluster area $n_{cl}(c_1, i')$ and those of background fields $n_f(c_1, i')$, for which we assumed that the distribution of background field stars on the C-M plane does not vary across the observed field. The local signal-to-noise ratio $s(c_1, i')$ in each subgrid element was then calculated by Equation (2), where g is simply the ratio of the area of the cluster region to that of the background field.

$$s(c_1, i') = \frac{n_{cl}(c_1, i') - gn_f(c_1, i')}{\sqrt{n_{cl}(c_1, i') + g^2 n_f(c_1, i')}} \quad (2)$$

From the array s , we obtained an optimal mask envelope in the (c_1, i') plane by setting a threshold $s_{lim} < s_{max}$ (maximum of s) and identifying the subgrid elements of $s \geq s_{lim}$. In order to do this, the elements of $s(c_1, i')$ were sorted into a series of gradually decreasing thresholds over the one-dimensional index k . From the determined subgrid element with the highest signal-to-noise ratio (s_{max}), a cumulative number of stars in the cluster area $N_{cl}(a_k) = \sum_{l=1}^k n_{cl}(l)$ was then counted through a progressively larger area $a_k = ka_l$, where a_l is the area of a single element of the C-M plane. The cumulative star counts for the background field $N_f(a_k) = \sum_{l=1}^k n_f(l)$ were calculated in the same manner as for the cluster area. The cumulative signal-to-noise ratio $S(a_k)$ was then determined by Equation (3):

$$S(a_k) = \frac{N_{cl}(a_k) - gN_f(a_k)}{\sqrt{N_{cl}(a_k) + g^2 N_f(a_k)}} \quad (3)$$

$S(a_k)$ reaches a maximum value for a particular subarea of the C-M plane, and the corresponding value of $s(c_1, i')$ is set to a threshold, i.e., s_{lim} . Now, the filtering mask area is chosen by selecting subgrid elements with larger $s(c_1, i')$ values than the determined s_{lim} . The heavy lines in (c_1, i') CMDs in Figure 2 represent the boundaries of the selected subgrid elements. The faint limits of the filtering mask areas were assigned to be $i' = 22.0$ for NGC 5466 and $i' = 22.5$ for the other clusters to avoid biases caused by the poor completeness ($\sim 70\%$) of the photometry and by the variable seeing conditions over the surveyed sky areas during the observations. Finally, the entire sample of stars in the determined filtering mask area was considered in the subsequent analyses to examine the spatial configuration around the target clusters.

4. SPATIAL CONFIGURATION OF STARS

In this section, we present and discuss the analytic results related to the spatial configuration of stars in the vicinity of target clusters individually for each cluster. Details of the extended tidal features with significant overdensities of stars over the limiting tidal radii of the clusters are examined by (1) the spatial surface density map of stars, (2) the radial profiles of the surface density, and (3) the azimuthal number density profiles as a function of position angle at various radial distances from the cluster center.

To construct a spatial surface density map, we first made a two-dimensional star count map by binning into small grids on the spatial stellar distributions of the C-M mask-selected stars for each cluster. The background density level was simply assigned by the measured mean surface density value for the region outside the tidal radius of each cluster since a variation with relatively low background density does not seriously affect to the two-dimensional configuration of stellar distribution around a cluster. The background-subtracted star count map was transformed into a smoothed surface density map by means of a Gaussian smoothing algorithm that enhanced the low spatial frequency of the background variation and removed the high frequency of the spatial stellar density variation. Then, we overlaid isodensity contour levels with a standard deviation unit (σ) of the background level on the smoothed maps with various kernel values.

As an analytic indicator to confirm the overdensity feature around the tidal radius of a cluster, the radial surface density profile of a cluster was derived by measuring the number of stars in concentric annuli with a $1.0'$ width. The effective radius of each annulus is assigned by the equation $r_e = \sqrt{0.5(r_i^2 + r_{i+1}^2)}$, where r_i and r_{i+1} are the inner and outer radii of an annulus, respectively. Radial surface density profiles for a different direction are also derived, for which we divided an annulus with $3.0'$ widths into eight sections (S1–S8) with an angle of 45° , as shown in Figure 4. Here, we caution that the

radial surface densities at the central region of cluster fields are usually underestimated by crowding effects. In order to examine the crowding effects, we added appropriate number of artificial stars with i magnitudes in the range of the C-M mask-selected area (Figure 2) to the i images of each cluster, and we calculated the mean radial recovery rates of the input artificial stars as completenesses in photometric measurements out to $\sim 25'$ from the cluster's center. Considering the determined photometric completenesses, we empirically fit the King (1966) models to the observed radial surface density profiles of target clusters over a radial range that keeps up recovery rates in stable with high completenesses. It is worth noting that McLaughlin & van der Marel (2005) have used the Wilson (1975) models to describe properly the outer surface density structure of the majority of globular clusters in the Galaxy and the Magellanic Clouds. It is true that the Wilson models are spatially extended more than the King (1966) models, but the Wilson models have still finite truncated tidal radii. This leads that the Wilson models are unlikely to describe extratidal overdensity features of globular clusters, which are usually characterized by a break and radially untruncated power laws of the surface density profiles.

Clusters with obvious extratidal extensions showed a break in the observed radial surface density profiles near the tidal radius (Grillmair et al. 1995; Leon et al. 2000; Testa et al. 2000; Rockosi et al. 2002; Lee et al. 2003; Olszewski et al. 2009), which departs from the form predicted by the King (1966) models. Numerical simulations also confirmed such a break with power laws in the radial surface density profiles due to the features of tidal debris around the clusters (e.g., Combes et al. 1999; Johnston et al. 1999, 2002). Indeed, Johnston et al. (1999) predicted that for a constant mass-loss rate, the radial surface densities of stripped stars in the tidal tails are proportional to r^{-1} . However, Rockosi et al. (2002) found that the annular-averaged density of stars along the well-defined extratidal tails around Pal 5 is fit to a power law with a significantly steeper slope than that predicted by Johnston et al. (1999). For the target clusters in this paper, we fit a power

law of r^γ to the outer part of radial profiles measured in full concentric annuli, and compare the measured slope (γ) with those of Rockosi et al. (2002) and Johnston et al. (1999). To investigate directions of the overdensity feature, we also measure slopes of power laws for the radial surface density profiles to eight angular sections with different directions.

The azimuthal number density of stars with respect to a position angle was also derived for stars in an assigned annulus. The position angle was measured clockwise from the east principal axis in a 10° unit. Widths of each annulus were assigned to be $10'$ and $15'$ for the inner and outer regions, respectively, in order to contain a statistically sufficient number of stars in each area. The radially cumulative azimuthal number density profile was also derived to trace the direction of the stellar overdensity feature around the clusters.

4.1. M15

Figure 5 shows a raw star count map around M15 and the surface density maps smoothed with various Gaussian kernel values of 0.09° , 0.135° , and 0.195° , from the upper-left panel to the lower-right panel. The spatial bin size of the star count map was originally set to be $1.8' \times 1.8'$. Several individual blank chips, which did not contain useful observational data in Figure 5, were excluded from the subsequent analyses. Isodensity plots were overlaid on the maps with the contour levels of 2σ , 2.5σ , 3σ , 4σ , 8σ , and 30σ above background density level, where σ is the standard deviation of the mean background value. Contours in the star count map are the same as those in the smoothed surface density map with a Gaussian kernel value of 0.195° . The different arrows indicate directions of the Galactic center (short arrow) and the projected absolute proper motion (long arrow), i.e., $\mu_\alpha \cos \delta = -0.30 \pm 1.00 \text{ mas yr}^{-1}$ and $\mu_\delta = -4.20 \pm 1.00 \text{ mas yr}^{-1}$ (Cudworth & Hanson 1993). The circle centered on the cluster indicates its tidal radius of $r_t = 21.5'$ (Harris 1996).

It is apparent in Figure 5 that the overdensity feature is obviously extended over the tidal radius of M15 at the levels larger than 2σ above the background. Furthermore, the extratidal overdensity feature beyond the tidal radius seem to form extended tails around the cluster. Among them, long tails to the southwest and northeast directions around the cluster are aligned apparently with the directions of the Galactic center and anticenter. Marginal extensions are present in the outskirts to the south and north directions, which could correspond to the cluster’s orbit. The overdensity feature of the tails becomes more prominent in the lower resolution surface density maps with a larger Gaussian kernel value. It is noted here that we did not find distinctive evidence for a southeast tidal extension as observed by Grillmair et al. (1995). The difference could be accounted for by the lower spatial resolution and the brighter photometric limiting magnitude used by them. Indeed, most of the cluster stars in this study are faint main-sequence stars, while Grillmair et al. (1995) used the subgiant branch stars and main-sequence stars near the turn-off point of the CMD. Note that Combes et al. (1999) certified in their simulation that low mass stars were usually stripped from a globular cluster and formed tidal tails or streams.

The radial surface densities for M15 measured in each concentric annulus are plotted in the upper panel of Figure 6 along with a theoretical King model of $c = 2.5$, which are arbitrarily normalized to our measurements. We also show two plots of the observed-minus-predicted residuals, $\log(O/C)$, to illustrate the departures of the observed radial surface densities from the prediction of the King model, and of the photometric recovery rates to consider radial crowding effects on the observed profile. It is apparent in the plots that incompleteness due to crowding effects reduces the measured surface densities in the innermost region, while the radial surface density profile in the region outer than $\log(r') \sim 0.7$ has completeness values larger than $\sim 95\%$. Consequently, the radial surface density profile departs from the King model with a break at a radius less than the tidal radius, i.e., $\sim 0.7r_t$, and the excess extends to $\sim 1.5r_t$. The radial surface density profile

in this overdensity region resembles a radial power law with a slope of $\gamma = -1.59 \pm 0.21$, which is comparable to the value -1.58 ± 0.07 proposed by Rockosi et al. (2002) from the annular-averaged densities of stars along the extratidal tails of Pal 5. However, the slope is significantly steeper than the case of $\gamma = -1$, predicted for a constant mass-loss rate over a long time (Johnston et al. 1999). Radial surface density profiles to eight angular sections with a different direction, as illustrated in Figure 4, are also represented in the lower panel of Figure 6. The overdensity feature in the region of $0.7r_t \lesssim r \lesssim 1.5r_t$ is commonly detected in all eight angular sections. The estimated mean surface densities (μ) in the angular sections 1, 4 and 8 are higher than those in the other sections. This is in good agreement with the extended overdensity features to the directions of the Galactic center and anticenter, as shown in the surface density maps of Figure 5. Comparing the power laws of the radial surface density profile in each angular section, the slopes (γ) seem to be shallower in angular sections 2 and 6, which are likely aligned with the orbit of M15, i.e., the direction of the cluster’s proper motion.

Figure 7 shows the annular and cumulative azimuthal number density profiles around M15. As presented in Figure 4, we measured the number density clockwise from the east principal axis with a 10° angular bin. Note that number densities at the angular bins without data, caused by the blank chips, are interpolated by the values of adjacent angular bins. The radial range $15' \leq r < 75'$ corresponds to $0.7r_t \lesssim r \lesssim 3.5r_t$, in which we examine the direction and the extension of the tail feature of M15. The radial bins are set to be $10'$ for the inner three annuli and $15'$ for the outer two annuli. At the innermost annulus with $15' \leq r < 25'$, it is apparent that the number densities in the ranges of position angles $\sim 150^\circ$ to $\sim 220^\circ$ and $\sim 300^\circ$ to $\sim 60^\circ$ are clearly higher than those in the other position angles. The high density features in the positions are likely to extend to the whole observed field on the sky, as shown in the cumulative azimuthal number density profile. This is in accordance with the tail features to the direction of the Galactic center and anticenter, as

shown in the surface density map of Figure 5. With a somewhat low confidence, there also seems to be relatively weak overdensity features at position angles $\sim 100^\circ$ and $\sim 280^\circ$ in the regions of the inner two annuli (i.e., $15' \leq r < 35'$). These are reliably matched with the tails to the direction along the cluster’s orbit, as inferred from the surface density maps and the radial density profiles of M15.

4.2. M30

In Figure 8 we show the spatial configuration of stars surrounding M30. The top-left panel shows the two-dimensional star count map that was made by measuring the number of cluster stars in each $2.5' \times 2.5'$ bin on the C-M mask-selected star count map of M30. The other panels to the bottom-right show the smoothed surface density maps with Gaussian kernel widths of 0.084° , 0.147° , and 0.210° . Note that in Figure 8 the Megacam observations were not secured at the outer southeast field of M30. The isodensity contours with the background level and 0.5σ , 1.5σ , 2.5σ , 3.5σ and 8σ levels above the background were overlaid on the surface density maps. Contour levels in the star count map correspond to those of a smoothed map with a Gaussian kernel width of 0.210° . The short arrow indicates the projected direction to the Galactic center on the sky, and the long arrow indicates the projected proper motion with $\mu_\alpha \cos \delta = 1.42 \pm 0.69 \text{ mas yr}^{-1}$ and $\mu_\delta = -7.71 \pm 0.65 \text{ mas yr}^{-1}$, measured by Dinescu et al. (1999). The tidal radius of M30 (i.e., $r_t = 18.34'$) from Harris (1996) was also plotted as a circle centered on the cluster.

At contour levels larger than 0.5σ above the background, it is apparent in Figure 8 that a flocculent overdensity feature with tails is well developed around M30 and extends to about $2r_t \approx 40'$ and beyond. While there is no strong evidence of extratidal features extending into specific directions in the surface density maps, the apparent east-west extension seems to be aligned with the direction of the Galactic center and anticenter.

There is no apparent extended extratidal tail toward the direction of the proper motion on the cluster’s orbit in the surface density maps. Instead, distant stars unbound from the cluster are likely building up a feature of the northern extension to the opposite direction of the cluster’s proper motion, with significant overdensities up to a contour level of 2.5σ in Figure 8. The northern extension feature is likely tracing the cluster’s trailing tail through its orbital path. We note, however, given the position and distance of M30 from the Galactic plane, the northern extension of the stars could be a result of gravitational interaction with the Galactic plane (Piotto et al. 1997).

A radial surface density profile for M30 was derived by measuring the mean number density of stars in concentric annuli and is presented in the upper panel of Figure 9. For the inner profile, we overplotted a theoretical King profile of $c = 2.5$, which was arbitrarily normalized to the observed radial surface density profile of M30. The observed-minus-predicted residuals illustrate the deviations of the observed radial surface densities from the prediction of the King model. The innermost region shows crowding effects out to $\log(r') \sim 0.5$, after which the photometric completenesses keep a nearly constant value of $\sim 98\%$. A break in the observed radial density profile appears at a radius less than the tidal radius of M30, i.e., $\sim 0.6r_t$, and the overdensity feature extends to about $2r_t$ of the cluster. The departure of the observed radial surface density profile in this region from the King profile is characterized by a power law with a slope of $\gamma = -1.41 \pm 0.21$. Similar to the case of M15, the slope is also significantly steeper than the index of r^{-1} predicted for extratidal structure with a constant mass-loss rate over a long time (Johnston et al. 1999). Radial surface density profiles to eight angular sections are plotted in the lower panel of Figure 9. Note that incompleteness due to crowding reduces the measured surface densities at the innermost point with respect to those expected by the King model. It is apparent that the profiles have in common a break at $\sim 0.6r_t$ and an extended overdensity feature to $\sim 2r_t$ with a power law. At the radial range, the estimated mean surface densities are relatively

higher in the angular sections 4 and 8 than in the other sections. This can be explained by the spatially extended extratidal features to the directions of the Galactic center and anticenter, as shown in the surface density map of Figure 8. We also note that the slopes of the radial density profiles of the angular sections 2 and 6 are shallower in the radial range of $0.6r_t \lesssim r \lesssim 2r_t$ than those of the other angular sections. This feature may be related to a cluster’s orbit inferred from the proper motion, although the spatial surface density maps do not show an extinctive extratidal feature of stars on the cluster’s orbit.

The left and right panels of Figure 10 show the annular and radially cumulative azimuthal number density profiles, respectively, of M30 with an angular bin of 10° . The radial bins are set to be $10'$ for the inner three annuli and $15'$ for the outer two annuli. The tidal radius of M30 is placed in the innermost annulus. As shown in Figure 10 the azimuthal number density profiles have a flocculent feature with respect to the position angle, which is also expected in the spatial surface density maps of Figure 8. Nevertheless, there appear to be two main overdensity ranges of the position angle, i.e., $\sim 120^\circ$ to $\sim 220^\circ$ and $\sim 300^\circ$ to $\sim 40^\circ$, in the azimuthal number density profile for the innermost annulus. Also, the overdensity feature in the ranges of the position angle extends to the second annulus, i.e. $\lesssim 2r_t$, with a somewhat low confidence. This might be associated with the apparent east-west extension of stars to the direction of the Galactic center and anticenter, as shown in the spatial surface density maps in Figure 8. In the azimuthal number density profiles, we did not find evidence of the extended extratidal features induced by the cluster’s orbital motion at the remote area in the vicinity of M30.

4.3. M53 and NGC 5053

Figure 11 represents the spatial configuration of selected stars in the vicinity of a pair of the two clusters M53 and NGC 5053. As described in Sections 2 and 3, cluster stars for

both clusters are selected by using the same selection criteria in C-M spaces of (c_1, i') and (c_2, i') . The upper-left panel is a raw star count map with a spatial bin size of $3.0' \times 3.0'$. The surface density maps smoothed with various Gaussian kernel values of 0.125° , 0.175° , and 0.240° are also plotted in Figure 11 to bottom-right. The long arrow indicates the direction of the proper motion of M53, and the two short arrows represent the direction to the Galactic center. The proper motions of M53, i.e., $\mu_\alpha \cos \delta = 0.50 \pm 1.00 \text{ mas yr}^{-1}$, $\mu_\delta = -0.10 \pm 1.00 \text{ mas yr}^{-1}$ are adopted from Dinescu et al. (1999). The proper motion of NGC 5053 has not yet been reported. Circles are tidal radii for each cluster, i.e., $r_t = 21.75'$ for M53 and $r_t = 13.67'$ for NGC 5053 (Harris 1996).

It is remarkable in Figure 11 that the spatial distribution of stars in the vicinity of M53 and NGC 5053 show a complex configuration with various extratidal features. The contour levels are background level, and 2σ , 4σ , 8σ , and 20σ above background level, where σ is the standard deviation of the estimated background level. The main new findings that were observed in the surface density maps are as follows: (1) the extratidal overdensity features extended over the tidal radii of both clusters at the contour levels above the background, (2) features of tails on the cluster's orbit in the east-west direction for M53 and to the direction of the Galactic center for NGC 5053, (3) complex substructures of extratidal feature of clumps and ripples around the clusters, (4) a tidal bridge-like structure connecting spatially the close neighbor pairing of M53 and NGC 5053, and finally (5) an envelope composed by stars surrounding the cluster system. Of particular interest are the tidal features that are possibly enhanced by the dynamical interaction between two clusters, which include features such as clumps and ripples surrounding the clusters and most strikingly, a tidal bridge-like feature and an envelope structure around the multiple globular cluster system. Note that there are no known binary globular clusters in the Milky Way, while Minniti et al. (2004) reported the discovery of a binary cluster in the peculiar giant elliptical galaxy NGC 5128. We therefore point out that these observed extratidal

structures of the pairing system of M53 and NGC 5053 could indeed play a unique key role in the effect of near passage on the dynamical tidal interaction between two globular clusters in the Galaxy.

The upper panel of Figure 12 shows the radial surface density profile of M53, which was derived by measuring mean stellar number densities in each concentric annulus. Stars within the tidal radius of the companion cluster NGC 5053 were not included in the radial surface density profile of M53 to avoid overlapping of stars in NGC 5053. In order to compare the observed radial density profile, a theoretical King model was computed with a concentration parameter $c = 1.78$. As apparent in Figure 12, the observed profile departs from the King model with a break at a radius less than the tidal radius, i.e., $0.7r_t$. Note that the surface densities in the innermost region is affected by crowding effects out to $\log(r') \sim 0.8$, after which the photometric completenesses show a nearly constant value of $\sim 98\%$, as shown in the plot of the radial photometric recovery rates. The overdensity feature, which extends to $1.6r_t$, is likely represented by a power law with a slope of $\gamma = -1.58 \pm 0.19$, which is almost identical with the value -1.58 ± 0.07 for the annular-averaged densities of stars in the extratidal tails of Pal 5 (Rockosi et al. 2002), but significantly steeper than that predicted from a constant orbit-averaged mass loss rate (Johnston et al. 1999). The residual plot within the tidal radius also exhibits a departure of the observed radial surface densities from the prediction of the theoretical King model. As a signature of the presence of tidally stripped stars, Beccari et. al. (2008) also recognized a change in slope of the radial surface density profile for M53.

The lower panel of Figure 12 shows radial surface density profiles of M53 in different directions. Of the total eight angular sections defined in Figure 4, we could not derive the radial profiles of the angular sections 5 and 6 because observational data were not secured for the southern area of M53. As can be seen from Figure 12, the obtained radial profiles for

the six angular sections show behaviors of a break at $\sim 0.7r_t$ in common, becoming power laws over the tidal radius to $1.6r_t$. This trend resembles the extended overdensity features over the tidal radius appearing in the surface density maps of Figure 11. The estimated mean densities (μ) at the radial range show higher values in the angular sections 1, 4, and 8. This feature corresponds to the apparent extratidal tails on the cluster’s orbit in the east-west direction around M53, as shown in Figure 11. Also, slopes (γ) of the power laws in the angular sections 3 and 4 seem to be slightly flatter than the mean slope of the radial surface density profile of M53. It can be noted that angular sections 3 and 4 are equivalent in the directions of the Galactic anticenter and the trailing tail on the cluster’s orbit.

In Figure 13, we show the annular and cumulative azimuthal number density profiles around M53 with a 10° angular bin. We have divided the total sample in the radial range of $15' \leq r \leq 75'$, which corresponds to $0.7r_t \lesssim r \lesssim 3.5r_t$, into five concentric annuli with radial bins with $10'$ and $15'$ widths for the inner three and outer two bins, respectively. The tidal radius of M53 is placed in the innermost annulus. The blank bins in Figure 13 correspond to the areas without photometric data and the area within the tidal radius of the neighbor cluster NGC 5053. The azimuthal density profiles for the two inner annuli indicate the overdensity feature in the range of position angles $\sim 160^\circ$ to $\sim 240^\circ$, which is in good agreement with the direction of the trailing tail on the cluster’s orbit. Also, an apparent overdensity feature in the range of position angles $\sim 310^\circ$ to $\sim 20^\circ$ likely traces the tidal bridge-like feature in the direction of the companion cluster NGC 5053, as shown in the surface density maps of Figure 11.

We now turn to NGC 5053, which is a very diffuse cluster with a low concentration parameter $c = 0.85$ (Harris 1996). Figure 14 shows the derived radial surface density profiles of NGC 5053. As in the case of the companion cluster M53, stars within the tidal radius of M53 were not used to derive the radial density profile of NGC 5053. The upper

panel shows the profile of the mean surface densities measured in each concentric annulus, and the lower panel consists of those of eight angular sections. The observed profiles were compared with a theoretical King model of $c = 0.85$. By crowding effects, surface densities seem to be reduced in the central region of the cluster inner than $\log(r') \sim 0.5$, after which the photometric completenesses show a nearly constant value of $\sim 96\%$. A break at $\sim 0.7r_t$ is commonly appeared in the obtained radial density profiles. The overdensity feature extended to $2.5r_t$ of NGC 5053. For the radial profiles measured in concentric annuli, the departure from the King model in this region can be represented by a power law with a slope $\gamma = -0.62 \pm 0.15$. It is remarkable that the radial surface density profiles of NGC 5053 are characterized by a long extension of the extratidal overdensity feature and a much shallower slope of the power law compared with the case of the slope $\gamma = -1$ in a constant mass-loss rate of Johnston et al. (1999). This is indeed consistent with the diffuse structure of the cluster with a small concentration of $c = 0.84$ (Harris 1996). In the overdensity region, the mean surface densities (μ) are higher in the angular sections 3 and 4, and the angular sections 7 and 8 than in the other angular sections. Angular sections 3 and 4 are coincident with the tidal bridge-like feature toward the neighbor cluster M53. Also, the high density in angular sections 7 and 8 might be related to the apparently extended extratidal features in the direction of the Galactic center, as shown in Figure 11.

Figure 15 shows the annular and radially cumulative azimuthal number density profiles around NGC 5053, as a function of position angle. The radial range $10' \leq r \leq 80'$ corresponds to $0.7r_t \lesssim r \lesssim 5.9r_t$, in which we set six concentric annuli. The blank bins correspond to the areas without photometric data and the area within the tidal radius of the neighbor cluster M53. It is apparent that the azimuthal number density profile shows a flocculent feature at the innermost annulus in which the tidal radius of the cluster is imbedded. Peaks in the range of position angle $\sim 100^\circ$ to $\sim 200^\circ$ represent the tidal bridge-like feature appearing in the surface density maps. An extratidal extension feature

toward the Galactic center is correlated with peaks in the range of $\sim 250^\circ$ to $\sim 50^\circ$ on the azimuthal number density profiles.

4.4. NGC 5466

To examine the spatial configuration of stars around NGC 5466, we first constructed a star count map, as shown in the top-left panel of Figure 16, with a spatial bin size of $2.88' \times 2.88'$ for $\sim 3^\circ \times 3^\circ$ total field of view. We then smoothed the star count map with Gaussian kernel widths of 0.168° , 0.264° , and 0.312° , yielding smoothed surface density maps shown in Figure 16. Isodensity contour levels in Figure 16 correspond to values of the background level and 1σ , 2σ , 3σ , 4σ , 6σ , 10σ , and 40σ above the background. Contour levels in the star count map correspond to those of a smoothed map with a Gaussian kernel width of 0.312° . The circle centered on the cluster indicates its tidal radius of $r_t = 20.98'$ (Lehmann & Scholz 1997).

As can be seen in Figure 16, an overdensity feature above the background level apparently extends beyond the tidal radius of NGC 5466. Moreover, the extending extratidal overdensity feature seems to form two tails in the southeast and in the northwest directions. The tails stretch out symmetrically to both sides of the cluster, tracing over $\sim 2^\circ$ of arc in the observed field. These are the same features reported by Belokurov et al. (2006a) and Grillmair & Johnson (2006) in which the orientation of the tails is consistent with the cluster's orbit, as judged from the proper motion data. Note that the long arrow in Figure 16 indicates the direction of the projected proper motion of NGC 5466, i.e., $\mu_\alpha \cos \delta = -3.90 \pm 1.00 \text{ mas yr}^{-1}$, $\mu_\delta = 1.00 \pm 1.00 \text{ mas yr}^{-1}$ (Odenkirchen et al. 1997), while the short arrow represents the direction of the Galactic center. The tails also weakly show an S-shape feature of tidal stripping for cluster stars, as appeared for Palomar 5 (Odenkirchen et al. 2003). There are clumpy overdensity features in the southern area of

the observed field, which were also found in the surface density map of Grillmair & Johnson (2006). However, neither the cluster’s orbit nor the direction to the Galactic center is likely to have a correlation with the clumpy structure. The appearance of such clumps can be caused either by the background galaxies or by the local substructures of the stars in the Galactic halo.

The upper panel of Figure 17 shows the radial surface density profile of NGC 5466, for which we measured mean stellar number densities in concentric annuli. The solid curve characterizes the empirical representation of the data fitted by the King model of $c = 1.2$. While the measured surface densities have a nearly constant completeness value of $\sim 98\%$, the very central region of the cluster inner than $\log(r') \sim 0.1$ seems to show crowding effects. Although the inner part of the profile is well represented by the King model, the observed profile departs from the model prediction at the radius of $\sim 0.5r_t$, showing the extended overdensity feature to be $\sim 2r_t$. The radial surface density profile in this region is characterized by a power law with a slope $\gamma = -2.44 \pm 0.13$. The measured slope is significantly steeper than the cases of a constant mass-loss rate $\gamma = -1$ (Johnston et al. 1999) and of the other target clusters in this paper. This is certainly because NGC 5466 shows a well-developed structure of extratidal tails. Indeed, Rockosi et al. (2002) found the annular-averaged surface densities of stars along the well-defined extratidal tails of Pal 5 are also fitted to a power law in radius with a significantly steeper slope. Lehmann & Scholz (1997) also found an increased surface density in the outer region of the radial density profile for NCG 5466, which may be an indication of a tidal tail caused by unbound stars around the cluster. The departure of the radial profile from the prediction of the King model is more obviously presented in the residual plot of Figure 17. The lower panel of Figure 17 shows the radial surface density profiles of eight angular sections in the observed field, as mentioned in Figure 4. The break at $\sim 0.5r_t$ and the increased density features out to $\sim 2r_t$ are shown in profiles for all eight angular sections, and are in good agreement

with the extratidal overdensity feature in the surface density maps of Figure 16. Also, the estimated mean surface densities (μ) of the radial range are relatively higher in angular sections 3, 4, and sections 7, 8 than in the other sections. This is clearly a consequence of the two tails in the southeast and in the northwest directions around the cluster, as shown in the Figure 16.

The orientation of the detected two tails is further analyzed in Figure 18, which shows annular (left panels) and radially cumulative (right panels) azimuthal number density profiles around NGC 5466. The area within the radial range of $15' \leq r < 75'$, i.e., $0.7r_t \lesssim r \lesssim 3.6r_t$ of NGC 5466, was divided into five concentric annuli with radial bins of $10'$ (inner three) and $15'$ (outer two) widths. We then clockwise measured the azimuthal number density with a 10° angular bin. It is apparent from the inner two annuli of the Figure 18 that there are two main overdensity ranges at the position angles $\sim 120^\circ$ to $\sim 210^\circ$ and $\sim 320^\circ$ to $\sim 30^\circ$, with peaks near 175° and 345° , respectively. The peaks seem to be slightly shifted to position angles $\sim 140^\circ$ and $\sim 330^\circ$ of the outer three annuli. These are well matched with the symmetric S-shape feature of the extratidal tails detected in the surface density maps of stars around NGC 5466, as shown in Figure 16.

5. Discussions and Summary

Using homogeneous wide-field observations obtained with the Megacam mosaic imager on the 3.6 m CFHT, we have undertaken several analyses to identify spatial configurations of stars surrounding five metal-poor globular clusters in the Galactic halo, i.e., M15, M30, M53, NGC 5053, and NGC 5466. Because of the low metallicities of the clusters we expected to easily detect the extratidal features from background stars with the secured wide-field deep photometric data covering an approximate $3^\circ \times 3^\circ$ field-of-view. Analyses of surface density maps revealed that all the clusters present features of extratidal overdensities

over their tidal radii in the form of extended tidal tails and halos around the clusters. The observed extratidal extensions likely trace the spatial orbits of the clusters as well as the effects of dynamical interaction with the Galaxy. Radial surface density profiles and azimuthal number density profiles confirmed the overdensity feature and the extratidal structure of tails and halos around the five metal-poor globular clusters.

M15, which is placed at 10.4 kpc from the Galactic center, is one of the densest globular clusters in the Milky Way. It is a post core-collapsed cluster (de Marchi & Paresce 1996) with a high concentration $c = 2.5$ (Harris 1996). Lauchner et al. (2006) pointed out that M15 is unlikely to have extratidal structures due to its high concentration. However, we found apparent extratidal features from the analyses of the spatial stellar distribution around M15. Indeed, surface density maps revealed features of tails in the directions of the Galactic center and anticenter and of tails in the direction of the cluster’s orbit inferred from the proper motion. The radial surface density profiles of stars surrounding M15 have a break at $\sim 0.7r_t$ and an excess of surface density extending to $\sim 1.5r_t$, which indicate tidal tail features around M15. Grillmair et al. (1995) and Lehmann & Scholz (1997) also found an indication for tidal tails in the radial stellar density profiles of M15. Radial surface density profiles in different directions and azimuthal number density profiles confirmed directions of the extended features of the tails around M15, which are seen in the surface density maps. From the results, we can conclude that the apparent tails around M15 are real tidal features of the cluster. No Abell clusters were found in the observed field, and the observed field was not polluted by a strong dust extinction ($E(B - V) = 0.10$). We note, however, that clumps in the observed field around M15 could be due to unidentified background galaxy clusters, although significant contamination by the clustered background objects seems a priori unlikely in the field (cf. Odenkirchen et al. 2001).

M30 is located on 7.1 kpc from the Galactic center. The cluster is one of the most

metal-poor globular clusters in the Milky Way with $[\text{Fe}/\text{H}] = -2.12$, and it has a very high concentration of $c = 2.5$ (Harris 1996). Extended extratidal features on the configuration of stars surrounding M30 have not yet been reported. Analyses of spatial surface density maps of stars in the vicinity of M30 revealed flocculent overdensity features with tails around the cluster that extend to about $2r_t$ and beyond. The radial surface density profiles of stars have a break at $\sim 0.6r_t$ for M30, and the surface density excess seems to extend to $\sim 2r_t$. The apparent east-west extension of the extratidal tails is likely associated with the direction of the Galactic center and anticenter. This is consistent with the extratidal overdensity property appearing in the radial surface density profiles and the azimuthal number density profiles for stars surrounding M30. Although tails associated with the direction of proper motion do not clearly show in the spatial surface density maps, the radial density profiles in $0.6r_t \lesssim r \lesssim 2r_t$ for M30 shows relatively shallower slopes with a power law in the direction of the cluster’s spatial orbit. We note, however, the visibility of such tails around M30 depends on the orientation of the cluster’s orbit to our line of sight, i.e., tails could not be observed if we were situated in the plane of a cluster’s orbit. The background features of galaxies and dusts are not likely to disturb the observed flocculent overdensity features of tails around M30. Indeed, the observed field is polluted only by two Abell clusters. The dust extinction is low toward this cluster ($E(B - V) = 0.03$) and the fluctuation of the dust emission is low as traced by the IRAS $100\mu\text{m}$ map.

The clusters M53 and NGC 5053 are close to each other, with a projected angular distance of about 1° , so they constitute an unusual astronomical pair in the outer halo of the Milky Way. These two clusters are the most metal-poor halo globular clusters with similar metallicities, i.e., $[\text{Fe}/\text{H}] = -1.99$ for M53 and $[\text{Fe}/\text{H}] = -2.29$ for NGC 5053. Also they have the same relative age as M92 (Heasley & Christian 1991; Rey et al. 1998) and a nearly the same distance modulus. The diffuse cluster NGC 5053 has a tidal radius of about $13.67'$ with a very low concentration parameter $c = 0.84$, while M53 has

a rather higher concentration $c = 1.78$ and a tidal radius of $21.75'$ (Harris 1996). In this study, we identified extratidal features on the spatial configuration of selected stars in the vicinity of two clusters M53 and NGC 5053. The observed tails likely trace the clusters' orbits and the direction to the Galactic center. As new findings, we detected features of clumps and ripples surrounding the clusters, and a tidal bridge-like feature and an envelope structure around the multiple globular cluster system. Here, we also note that Lauchner et al. (2006) reported a discovery of a 6° tidal stream extending from NGC 5053 in the southwest direction, using the SDSS data from which they removed stars within the tidal radius of M53 from the analysis. Unfortunately, it is difficult to confirm the extended stream in the surface density maps of Figure 11, because our observations do not contain photometric data in the southwest direction of the M53 and NGC 5053 system. Such spatial stellar configuration features might be a result of tidal interaction or merging between the two clusters. Indeed, the structures of clumps and ripples are predicted from recent numerical simulations for the interaction of two globular clusters (e.g., Miocchi et al. 2006). Furthermore, features such as a tidal bridge and an envelope in a multiple globular cluster system are also predicted from the numerical simulations of the possible merging of a set of globular clusters (e.g., Capuzzo Dolcetta & Miocchi 2008). From an observational point of view, van den Bergh (1996) suggested that a merging of clusters would occur more preferentially in dwarf galaxies with low velocity dispersions of the cluster system in the range of $6.5\sim 11 \text{ km s}^{-1}$ (Mateo 1996) rather than in the Milky Way.

To test the contamination of background galaxies in the field of M53 and NGC 5053, we analyzed the spatial distribution of non-pointlike SDSS sources. For the extracted SDSS sources, we transformed the SDSS $g'r'i'$ magnitude system into c_1 and c_2 indices, using the Equation (1). Sources falling into the masks in (c_2, i') and (c_1, i') planes, which were used to select cluster member stars, were applied to the sample of background galaxies. In Figure 19, we show a smoothed surface density map of the selected background galaxies,

overlaid with the surface density contours of cluster stars of Figure 11. Filled triangles indicate two Abell clusters in the observed field. As can be seen in Figure 19, we found no strong correlation between the pattern of the surface density variation of the background galaxies and the observed spatial configuration of stars around M53 and NGC 5053. Also note that the dust extinction is low toward the clusters (i.e., $E(B - V) = 0.02$ for M53 and $E(B - V) = 0.04$ for NGC 5053), and the variation in dust emission through the observed field is low as traced by the IRAS 100 μm map.

According to photometric results in this paper, it could be suggestive that the clusters M53 and NGC 5053 may be interacting or have interacted in the past. In the kinematic point of view, however, it would not be airtight that they originated with a same common dwarf spheroidal parent. The radial velocity of M53 is $-79.1 \pm 4.1 \text{ km s}^{-1}$, but it is $+44.0 \pm 0.4 \text{ km s}^{-1}$ for NGC 5053 (Harris 1996). In this case, the clusters might have a common space orbit to the similar direction, only if the tangential velocities are in same directions with exorbitantly larger values than their absolute values of radial velocities. The tangential velocity of M53 is estimated to be $\mu = 43.1 \pm 84.0 \text{ km s}^{-1}$ by using values of the proper motion, i.e., $\mu_\alpha \cos \delta = 0.50 \pm 1.00 \text{ mas yr}^{-1}$ and $\mu_\delta = -0.10 \pm 1.00 \text{ mas yr}^{-1}$ (Dinescu et al. 1999). Even if we are taking into account of the large measurement error, the calculated tangential velocity of M53 is merely comparable to the absolute value of the radial velocity. Unfortunately, we can not estimate the tangential velocity of NGC 5053 because the proper motion has not yet been reported. Thus, the current kinematic information about radial velocities and inaccurate tangential motions of M53 and NGC 5053 makes it still hard to arrange if the clusters came from a common dwarf and were on similar paths through the Galactic halo. Also, their distance moduli, $(m - M)_v = 16.31$ for M53 and 16.19 for NGC 5053 (Harris 1996), are still separated by $\sim 1.4 \text{ kpc}$, a significant distance in the halo of the Milky Way compared with their tidal radii 112.7 pc for M53 and 66.8 pc for NGC 5053 (Harris 1996). Nevertheless, it should be noted that radial

velocities of M53 and NGC 5053 are commensurate with those of the other clusters aligned in the Magellanic plane (see Figure 4c in Yoon & Lee 2002). Indeed, radial velocities of the globular clusters in the plane show a sinusoidal pattern of Keplerian motion as they are plotted against the orbital longitude measured along the Magellanic plane. This is possibly indicative of a common origin of the clusters.

The cluster NGC 5466 is at a 16.2 kpc distance from the Galactic center. It is one of the low-metallicity clusters with $[\text{Fe}/\text{H}] = -2.22$, and it has a low concentration with $c = 1.2$ (Harris 1996). Lehmann & Scholz (1997) found evidence of tidal tails around NGC 5466 in a radial density profile of the cluster. Recently, Belokurov et al. (2006b) observed tidal tails of NGC 5466, stretching about 2° in apposite directions. Using SDSS photometric data, Grillmair & Johnson (2006) found evidence for a much larger extension of the tidal tails, with the leading arm over $\sim 30^\circ$ and the trailing arm extending at least 15° . From numerical simulations, Fellhauer et al. (2007) reproduced the tidal tails around cluster NGC 5466. In our study, analyses for spatial configuration of stars around NGC 5466 have indicated an overdensity feature extending outside the tidal radius of the cluster. In the spatial surface density maps in Figure 16, we have found an S-shape extratidal feature of tails stretching out symmetrically over $\sim 2^\circ$ in the observed field. The observed radial density profiles of NGC 5466, as shown in Figure 17, show a departure from the King model, with a break at $\sim 0.5r_t$ extending the overdensity feature out to $\sim 2r_t$ of the cluster. Azimuthal number density profiles in Figure 18 confirmed the orientation of the two tails around NGC 5466, which is likely consistent with the cluster’s orbit inferred from the cluster’s proper motion. The results are reconfirmation of the tidal tails of NGC 5466 stretching as much as 45° on the sky as reported by Belokurov et al. (2006b) and Grillmair & Johnson (2006).

Similar to the case of M53 and NGC 5053, we checked contamination of background

galaxies in the field of NGC 5466 by analyzing the spatial distribution of non-pointlike SDSS sources. Figure 20 shows a smoothed surface density map of the selected background galaxies overlaid with the surface density contours of cluster stars from Figure 16. Filled triangles indicate eight Abell clusters in the observed field. As shown in Figure 20, the pattern of density variations in the selected galaxy sample does not seem to be correlated with the location of the tidal tails around NGC 5466. However, the spatial configuration of the selected background galaxies in the southern area of the observed field is likely correlated with the clumpy overdensity feature of the surface density maps of selected cluster member stars of Figure 16. The observed field is not polluted by strong dust extinction ($E(B - V) = 0.00$).

The other two low-metallicity clusters M68 and M92 in the Magellanic plane, for which we did not secure the wide-field deep photometric data from the present observations, are located on 10.1 kpc and 9.6 kpc from the Galactic center. Indications of extratidal extensions of stars around the clusters incidently have been overlooked in a few previous studies. Testa et al. (2000) used the DPOSS plates to show an circular structure of extratidal halo around M92 extending out to $\sim 30'$ from the cluster center. Also, Lee et al. (2003) used CFHT mosaic CCD imaging to discover a presence of extratidal materials in the radial density profile of M92 and a weak tidal halo around the cluster. In addition, Grillmair et al. (1995) found an indication for extratidal overdensity feature around M68 using photographic plates taken at the UKST. Nevertheless, there have been little evidences for extratidal tails toward any preferred directions on the spatial stellar distributions around both of the clusters because of the lower spatial resolutions and the brighter limiting magnitudes of the photographic and CCD photometry. Thus we note the need for deeper wide-field CCD photometry to investigate spatial structure of the extended extratidal tails around both of the clusters.

The spatial configuration of stars tidally stripped from a parent stellar system of a present globular cluster contains direct information of the dynamical evolution that the cluster has experienced. Along with internal dynamical processes, external perturbations, such as disk and bulge shocks by the Galaxy, could accelerate the cluster’s dynamical evolution (e.g., Spitzer & Hart 1971; Gnedin & Ostriker 1997). With respect to external dynamical evolution, three clusters, M15, NGC 5053 and NGC 5466 among our five targets might have experienced strong interactions with the Galaxy in the form of disk and bulge shocks, as indicated by the ratios of destruction rates with $v_{tot}/v_{evap} = 3.3, 130,$ and $160,$ respectively, for each cluster (Gnedin & Ostriker 1997). Here, v_{tot} and v_{evap} are the total destruction rate and the evaporation rate per Hubble time, respectively. Furthermore, Leon et al. (2000) suggested that tidal tails usually stretch into the Galactic center, as the effect of both bulge and disk shock or the bulge shock to the cluster is much stronger than disk shock for the cluster. This implies that tidal tails stretching into the Galactic center and anticenter around the three clusters M15, NGC 5053 and NGC 5466 might be a result of both the bulge and disk shock of the Galaxy. Two other clusters, M30 and M53, are not expected to suffer strong gravitational shocks by the Galaxy, with $v_{tot}/v_{evap} = 1.0$. This would be a reason why the tidal tail feature of M30 is not well defined in the direction of the Galactic center. Also, the tidal bridge-like feature and an envelope structure around M53 may not be the results of gravitational shocks of the Galaxy but the interaction with the companion cluster NGC 5053. In addition, apparent extratidal extensions around the other two globular clusters M68 and M92 with $v_{tot}/v_{evap} = 1.37$ and $1.00,$ respectively, may not be the results of suffering strong gravitational shocks by the Galaxy. In spite of such a dependency on the Galactic potential to the dynamical structure of the observed tidal tails, we found here that the feature of extratidal extensions around the target clusters is unlikely to have any distinctive correlation with the Galactocentric distance of each cluster.

On the other hands, many numerical simulations of tidal tails performed over the

past decade (i.e., Combes et al. 1999; Yim & Lee 2002; Capuzzo Dolcetta et al. 2005; Montouri et al. 2007) have suggested that the stars dissolved from a globular cluster by the Galactic tidal force slowly drift along the cluster’s orbit due to the orbital motion and the coriolis acceleration, and then eventually form a dense tidal tail parallel to the cluster’s orbit. In this paper, we found that all of the observed low-metallicity clusters have shown possible extratidal extensions to the direction of the clusters’ orbits, which are inferred from their proper motions. Indeed, the five target globular clusters are assumed to lie on one spatial orbital plane in the outer Galactic halo, and their kinematic motions place also almost on this plane (Yoon & Lee 2002), which are considered as a result of accretion of dwarf galaxies. Based on a comparison of population and kinematics, Yoon & Lee (2002) suggested that LMC is the possible parent galaxy of these halo globular clusters. However, recent studies (Palma et al. 2002; Bellazzini et al. 2003; Martinez-Delgado et al. 2004) have stated that M53, NGC 5053 and NGC 5466 are possible former members of the Sgr galaxy. To examine a possible association of the clusters with the Sgr orbit or Magellanic debris plane, we mark the three clusters on the planes formed by the rectangular Galactocentric coordinates with X, Y , and Z in kiloparsecs, as shown in Figure 21. The Magellanic debris plane (Yoon & Lee 2002) and the Sgr orbit (Ibata & Lewis 1998) are also overlaid in Figure 21. We also plotted the space motion vectors of two clusters M53 and NGC 5466 with the uncertainties in directions, in order to see their velocity coherence to the two orbital planes. Space motion vector of NGC 5053 is not plotted, since the proper motion of the cluster is not available. As shown in Figure 21, M53 is likely to move in a direction along the Magellanic plane. The space motion of M53 is perpendicular to the Sgr orbit in $X - Y$ plane, and it is directionally opposite in $X - Z$ plane to the orbital direction of the Sgr dwarf. The space motion vector of NGC 5466 in $X - Z$ plane seems to be parallel to the direction of the Sgr orbit, but it is not conclusive that NGC 5466 is moving along the Sgr orbit. The space motion of NGC 5466 in $X - Y$ plane is against the Sgr orbit, and it seems

to move in a direction along to the Magellanic plane within the uncertainty order of $\sim 2.5\sigma$ (e.g., Yoon & Lee 2002). In addition, NGC 5466 is closer in space to the Magellanic plane than to the Sgr orbit. NGC 5053 lies remarkably closer to the Magellanic plane than to the Sgr orbit, while it has no information about the space motion. These lead us to conclude that the three clusters M53, NGC 5053, and NGC 5466, are potentially associated with the Magellanic plane rather than the Sgr orbit.

Under these observational conditions, tidal tails for the five target globular clusters are expected to have a common feature of kinematic orbital properties, which would provide information about their parent dwarf galaxies. Although the spatial extensions and morphological shapes exhibited different regimes of developments for the observed extratidal tails, all the observed target clusters presented evidences of tidal tails tracing their orbits, as inferred from the projected directions of their proper motions. Thus, it appears that the tidal tails to the cluster’s orbit for five target metal poor halo clusters are indeed evidences for an accreted origin from satellite system. Also, these observational results of extratidal tail features around the five target clusters provide further evidences of the merging scenario of the formation for the Galactic halo, and in addition an important constraint on the potential in the Galactic halo (Odenkirchen et al. 2009).

Data for more accurate proper motions of target clusters and radial velocities of stars in the observed extratidal structures are essential to verify their association with a stream in the Galactic halo. Furthermore, larger area coverage with accurate deep photometric data will also enable us to better constrain the orbits of the target clusters and cluster’s member stars in the extratidal structures. With information about the spatial positions, radial velocities and proper motions of stars in the tidal tails, we could integrate their orbits backwards in the Galactic potential and eventually ascertain the origin of the globular clusters in the Galactic halo.

We are grateful to an anonymous referee for a detailed report that greatly improved this paper. This work has been supported by the Korea Research Foundation Grant funded by the Korea Government (KRF 2007-313-C00321), for which we are grateful.

REFERENCES

- Abadi, M. G., Navarro, J. F., & Steinmetz, M. 2006, MNRAS, 365, 747
- Aguilar, L., Hut, P., & Ostriker, J. P. 1988, ApJ, 335, 720
- Baumgardt, H., & Makino, J. 2003, MNRAS, 340, 227
- Beccari, G., et. al. 2008, ApJ, 679, 712
- Bellazzini, M., Ferraro, F. R., & Ibata, R. 2003, AJ, 125, 188
- Belokurov, V., et al. 2006a, ApJ, 642, L137
- Belokurov, V., Evans, N. W., Irwin, M. J., Hewett P. C., & Wilkinson, M. I. 2006b, ApJ, 637, 29
- Blumenthal, G. R., Faber, S. M., Primack, J. R., & Rees, M. J. 1984, Nature, 311, 517
- Bullock, J. S., & Johnston, K. V. 2005, ApJ, 635, 931
- Bullock, J. S., Kratsov, A. V., & Weinberg, D. H. 2001, ApJ, 548, 33
- Capuzzo Dolcetta, R., Di Matteo, P., & Miocchi, P. 2005, AJ, 129, 1906
- Capuzzo Dolcetta, R., & Miocchi, P. 2008, ApJ, 681, 1136
- Combes, F., Leon, S., & Meylan, G. 1999, A&A, 352, 149
- Cudworth, K. M., & Hanson, R. B. 1993, AJ, 105, 168
- Davis, M., Efstathiou, G., Frenk, C. S., & White, S. D. M. 1985 ApJ, 292, 371
- Dehnen, W., Odenkirchen, M., Grebel, E. K., & Rix, H.-W. 2004, AJ, 127, 2753
- de Marchi, G., & Paresce, F. 1996, ApJ, 467, 658

- di Matteo, P., Capuzzo Dolcetta, R., & Mocchi, P. 2005, *Celest. Mech. Dyn. Astron.*, 91, 59
- Dinescu, D. I., Girard, T. M., & van Altena, W. F. 1999, *AJ*, 117, 1792
- Fellhauer, M., Evans, N. W., Belokurov, V., Wilkinson, M. I., & Gilmore, G. 2007, *MNRAS*, 380, 749
- Ghigna, S., Moore, B., Governato, F., Lake, G., Quinn, T., & Stadel, J. 1998, *MNRAS*, 300, 146
- Ghigna, S., Moore, B., Governato, F., Lake, G., Quinn, T., & Stadel, J. 2000, *ApJ*, 544, 616
- Gnedin, O. Y., Lee, H. M., & Ostriker, J. P. 1999, *ApJ*, 522, 935
- Gnedin, O. Y., & Ostriker, J. P. 1997, *ApJ*, 474, 223
- Grillmair, C. J., Ajhar, E. A., Faber, S. M., Baum, W. A., Holtzman, J. A., Lauer, T. R., Lynds, C. R., & O’Neil, E. J., Jr. 1996. *AJ*, 111, 2293
- Grillmair, C. J., & Dionatos, O. 2006, *ApJ*, 643, L17
- Grillmair, C. J., Freeman, K. C., Irwin, M., & Quinn, P. J. 1995, *AJ*, 109, 2553
- Grillmair, C. J., & Johnson, R. 2006, *ApJ*, 639, 17
- Harris, W. E. 1996, *AJ*, 112, 1487
- Heasley, J. H., & Christian, C. A. 1991, *AJ*, 101, 967
- Ibata, R. A., Gilmore, G., & Irwin, M. J. 1994, *Nature*, 370, 194
- Ibata, R. A., Gilmore, G., & Irwin, M. J. 1995, *MNRAS*, 277, 781
- Ibata, R. A., & Lewis, G. F. 1998, *ApJ*, 500, 575

- Ibata, R., Irwin, M., Lewis, G. F., & Stolte, A. 2001a, *ApJ*, 547, L133
- Ibata, R., Irwin, M., Lewis, G., Ferguson, A. M. N., & Tanvir, N. 2001b, *Nature*, 412, 49
- Ibata, R. A., Wyse, R. F. G., Gilmore, G., Irwin, M. J., & Suntzeff, N. B. 1997, *AJ*, 113, 634
- Ivezić, Ž., et al. 2000, *AJ*, 120, 963
- Johnston, K. V. 1998, *ApJ*, 495, 297
- Johnston, K. V., Choi, P. I., & Guhathakurta, P. 2002, *AJ*, 124, 127
- Johnston, K. V., Sigurdsson, S., & Hernquist, L. 1999, *MNRAS*, 302, 771
- Jurić, M., et al. 2008, *ApJ*, 673, 864
- King, I. R. 1966, *AJ*, 71, 64
- Klypin, A., Kravtsov, A. V., Valenzuela, O., & Prada, F. 1999, *ApJ*, 522, 82
- Koch, A., Grebel, E. K., Odenkirchen, M., Martinez-Delgado, D., & Caldwell, J. A. R. 2004, *AJ*, 128, 2274
- Kundic, T., & Ostriker, J. P. 1995, *ApJ*, 438, 702
- Kupper, A. H. W., MacLeod, A., & Heggie, D. C. 2008, *MNRAS*, 387, 1248
- Lauchner, A., Powell, W. L., & Wilhelm, R. 2006, *ApJ*, 651, 33
- Lee, Y.-W., Joo, J.-M., Sohn, Y.-J., Rey, S.-C., Lee, H.-C., & Walker, A. R. 1999, *Nature*, 402, 55
- Lee, K. H., Lee, H. M., Fahlman, G. G., & Lee, M. G. 2003, *AJ*, 126, 815
- Lee, K. H., Lee, H. M., & Sung, H. 2006, *MNRAS*, 367, 646

- Lee, Y.-W., Gim, H. B., & Casetti-Dinescu, D. I. 2007, *ApJ*, 661, L49
- Lehmann, I., & Scholz, R.-D. 1997, *A&A*, 320, 776
- Leon, S., Meylan, G., & Combes, F. 2000, *A&A*, 359, 907
- Lynden-Bell, D. 1982, *The Observatory*, 102, 202
- Magnier, E. A., & Cuillandre, J.-C. 2004, *PASP*, 116, 449
- Martin, N. F., Ibata, R. A., Bellazzini, M., Irwin, M. J., Lewis, G. F., & Dehnen, W. 2004, *MNRAS*, 348, 12
- Martinez-Delgado, D., Butler, D. J., Rix, H.-W., Franco, V. I., Peñarrubia, J., Alfaro, E. J., & Dinescu, D. I. 2005, *ApJ*, 633, 205
- Martinez-Delgado, D., Dinescu, D. I., Zinn, R., Tutsoff, A., Cotié, P., & Boyarchuck, A. 2004, in *ASP Conf. Ser. 327, Satellites and Tidal Streams*, ed. F. Prada, D. Martinez-Delgado, & T. J. Mahoney (San Francisco: ASP), 255
- Majewski, S. R., Skrutskie, M. F., Weinberg, M. D., & Ostheimer, J. C. 2003, *ApJ*, 599, 1082
- Mateo, M. 1996, in *ASP Conf. Ser. 92, Formation of the Galactic Halo...Inside and Out*, ed. H. Morrison & A. Sarajedini (San Francisco: ASP), 434
- McLaughlin, D. E., & van der Marel, R. P. 2005, *ApJS*, 161, 304
- Minniti, D., Rejkuba, M., Funes, J. G., & Kennicutt, R. C., Jr. 2004, *ApJ*, 612, 215
- Miocchi, P., Capuzzo Dolcetta, R., Di Matteo, P., & Vicari, A. 2006, *ApJ*, 644, 940
- Monet, D. G., et al. 2003, *AJ*, 125, 984

- Montouri, M., Capuzzo Dolcetta, R., Di Matteo, P., Lepinette, A., & Mocchi, P. 2007, *ApJ*, 659, 1212
- Moore, B., Diemand, J., Madau, P., Zemp, M., & Stadel, J. 2006, *MNRAS*, 368, 563
- Moore, B., Ghigna, S., Governato, F., Lake, G., Quinn, T., Stadel, J., & Tozzi, P. 1999, *ApJ*, 524, L19
- Murali, C., & Weinberg, M. D. 1997, *MNRAS*, 291, 717
- Newberg, H. J., et al. 2002, *ApJ*, 569, 245
- Newberg, H. J., et al. 2003, *ApJ*, 596, L191
- Newberg, H. J., Yanny, B., & Willett, B. A. 2009, *ApJ*, 700, L61
- Odenkirchen, M., Brosche, P., Geffert, M., & Tucholke, H.-J. 1997, *New Astron.*, 2, 477
- Odenkirchen, M., et al. 2001, *ApJ*, 548, L165
- Odenkirchen, M., et al. 2003, *AJ*, 126, 2385
- Odenkirchen, M., Grebel, E. K., Kayser, A., Rix, H.-W., & Dehnen, W. 2009, *AJ*, 137, 3378
- Olszewski, E. W., Saha, A., Knezek, P., Subramaniam, A., de Boer, T., & Seitzer, P. 2009, *AJ*, 138, 157
- Ostriker, J. P., Spitzer, L., Jr., & Chevalier, R. A. 1972, *ApJ*, 176, L51
- Palma, C., Majewski, S. R., & Johnston, K. V. 2002, *ApJ*, 564, 736
- Piotto, G., Cool, A. M., & King, I. R. 1997, *AJ*, 113, 1345
- Rey, S.-C., Lee, Y.-W., Byun, Y.-I., & Chun, M.-S. 1998, *AJ*, 116, 1775

- Rocha-Pinto, H. J., Majewski, S. R., Skrutskie, M. F., Crane, J. D., & Patterson, R. J. 2004, *ApJ*, 615, 732
- Rockosi, C. M., et al. 2002, *AJ*, 124, 349
- Sbordone, L., Bonifacio, P., Marconi, G., Buonanno, R., & Zaggia, S. 2005, *A&A*, 437, 905
- Schlegel, D. J., Finkbeiner, D. P., & Davis, M. 1998, *ApJ*, 500, 525
- Searle, L., & Zinn, R. 1978, *ApJ*, 225, 357
- Siegel, M. H., Majewski, S. R., Cudworth, K. M., & Takamiya, M. 2001, *AJ*, 121, 935
- Smith, J. A., et al. 2002, *AJ*, 123, 2121
- Sohn, Y.-J., Park, J.-H., Rey, S.-C., Lee, Y.-W., Kim, H.-I., Oh, S. J., Lee, S.-G., Lee, M. G., & Han, W. 2003, *AJ*, 126, 803
- Spitzer L., Jr. & Hart M. H. 1971, *ApJ*, 166, 483
- Stetson, P. B. 1987, *PASP*, 99, 191
- Stetson, P. B. 1990, *PASP*, 102, 932
- Stetson, P. B. 1992, in *IAU Colloq. 136, Stellar Photometry: Current Techniques and Future Developments*, ed. C. J. Butler & I. Elliot (Cambridge: Cambridge Univ. Press), 291
- Stetson, P. B., & Harris, W. E. 1988, *AJ*, 96, 909
- Tautvaišienė, G., Wallerstein, G., Geisler, D., Gonzalez, G., & Charbonnel, C. 2004, *AJ*, 127, 373
- Testa, V., Zaggia, S. R., Andreon, S., Longo, G., Scaramella, R., Djorgovski, S. G., & de Carvalho, R. 2000, *A&A*, 356, 127

- Tormen, G. 1997, MNRAS, 290, 411
- Tormen, G. 1998, MNRAS, 297, 648
- Tormen, G., Diaferio, A., & Syer, D. 1998, MNRAS, 299, 728
- van den Bergh, S. 1996, ApJ, 471, L31
- van den Bergh, S. 2000, ApJ, 530, 777
- White, S. D. M., & Rees, M. J. 1978, MNRAS, 183, 341
- Wilson, C. P. 1975, AJ, 80, 175
- Yanny, B., et al. 2000, ApJ, 540, 825
- Yanny, B., et al. 2003, ApJ, 588, 824
- Yim, K.-J., & Lee, H. M. 2002, J. Korean Astron. Soc., 35, 75
- Yoon, S.-J., & Lee, Y.-W. 2002, Science, 297, 578

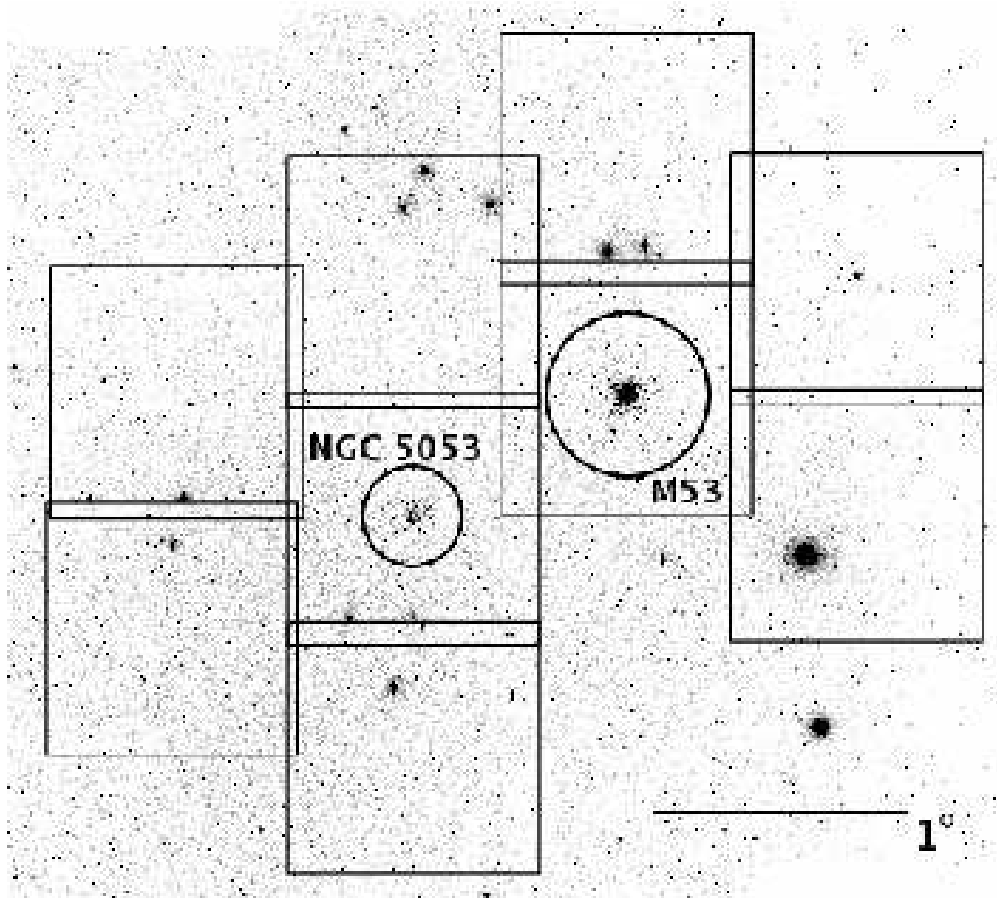


Fig. 1.— The Digitized Sky Survey image for the field of M53 and NGC 5053. Boxes represent the observed nine Megacam fields. Circles indicate the tidal radii for each cluster. North is up and east to the left.

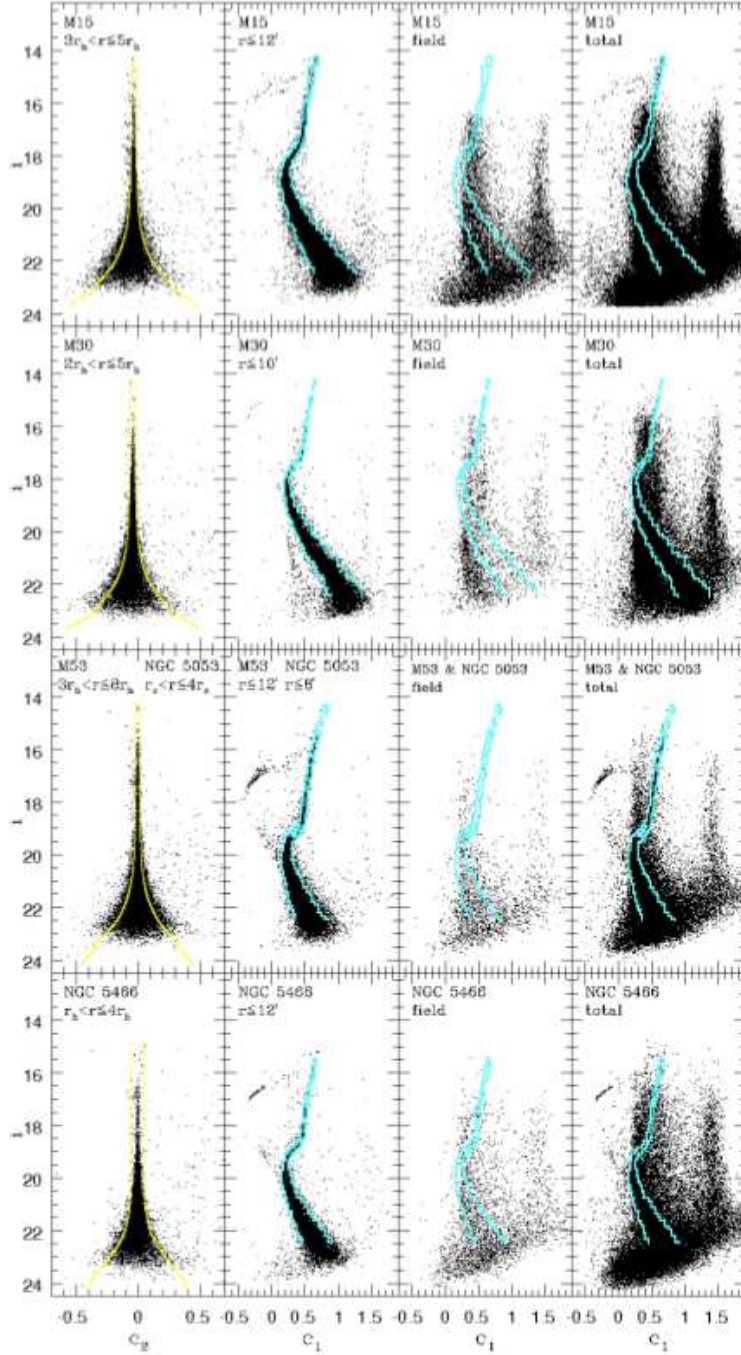


Fig. 2.— The (c_2, i') and (c_1, i') color-magnitude diagrams of stars in the fields of five target globular clusters. From left to right, the first panel is the (c_2, i') plane for stars in the empirically determined central regions of each cluster, the second to fourth panels are the (c_1, i') planes for stars in the clusters central area, in the assigned background fields, and in the total observed field, respectively. The lines in the (c_2, i') plane indicate $2\sigma_{c_2}$ limits at i' magnitudes due to photometric error. The lines in the (c_1, i') planes are the selected subgrid area determined through the mask filtering method

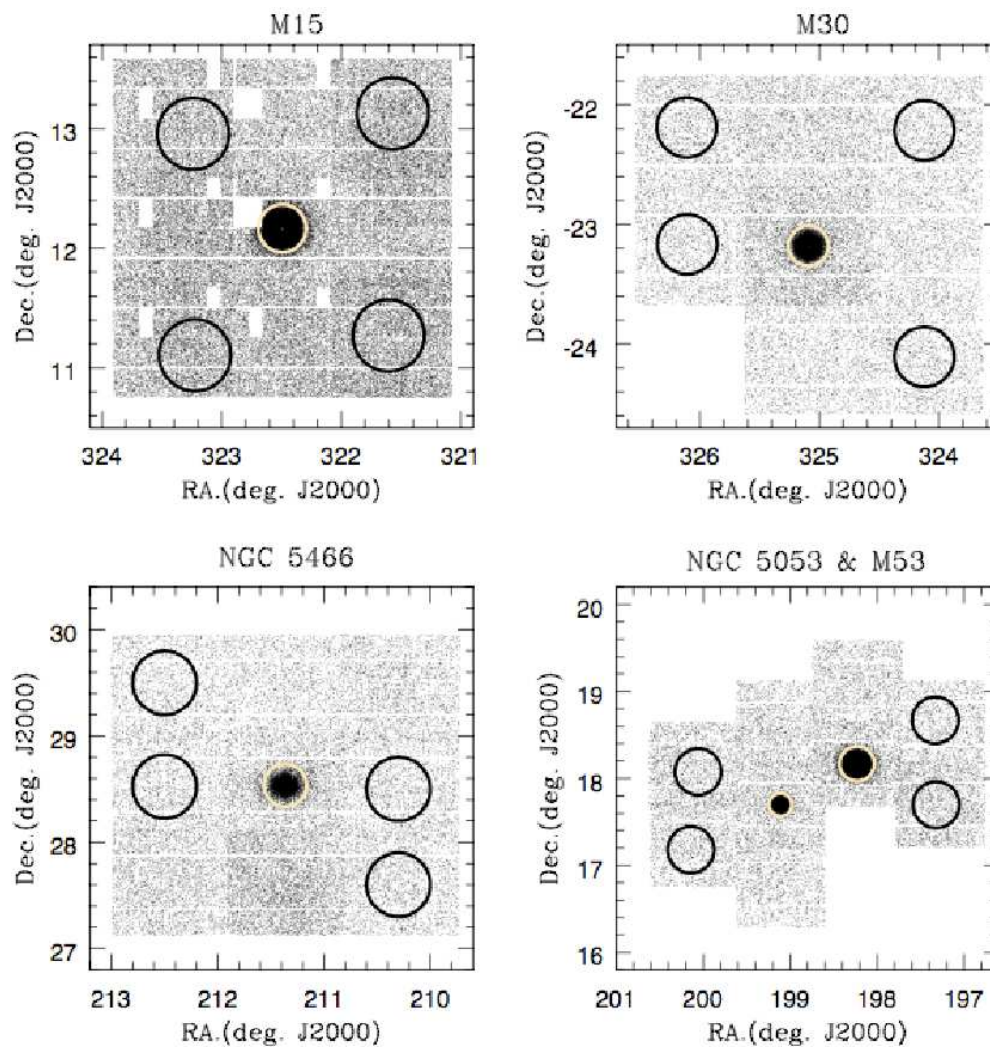


Fig. 3.— Spatial distribution of all stars measured in the vicinity of five globular clusters. Circles centered on each cluster indicate the cluster’s central areas in which the number ratio of stars enclosed in $2\sigma_{c_1}(i')$ and those outside of $2\sigma_{c_1}(i')$ in the (c_1, i') plane in Figure 2 has a maximum value. The other four circles in each field indicate the background areas for gauging the field star contamination.

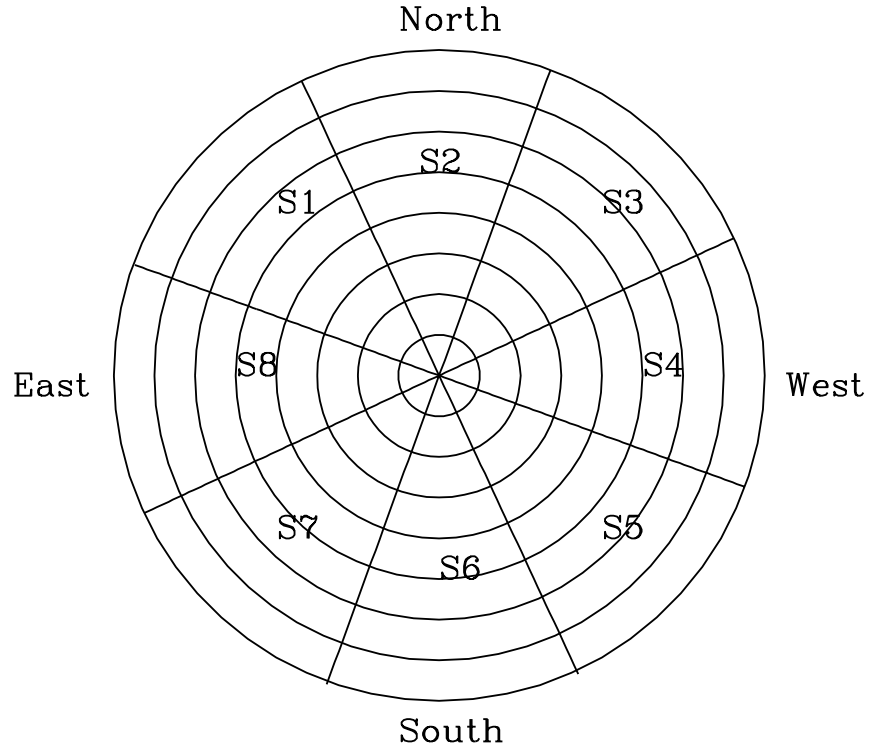


Fig. 4.— The schematic reseau plot used for the star counts. The radial surface densities were measured in concentric annuli. Each annulus was divided into eight angular sections (S1~S8) to derive surface density profiles for a different direction. Azimuthal number densities were determined in an assigned annulus with respect to a position angle measured clockwise from the east principal axis with a 10° unit.

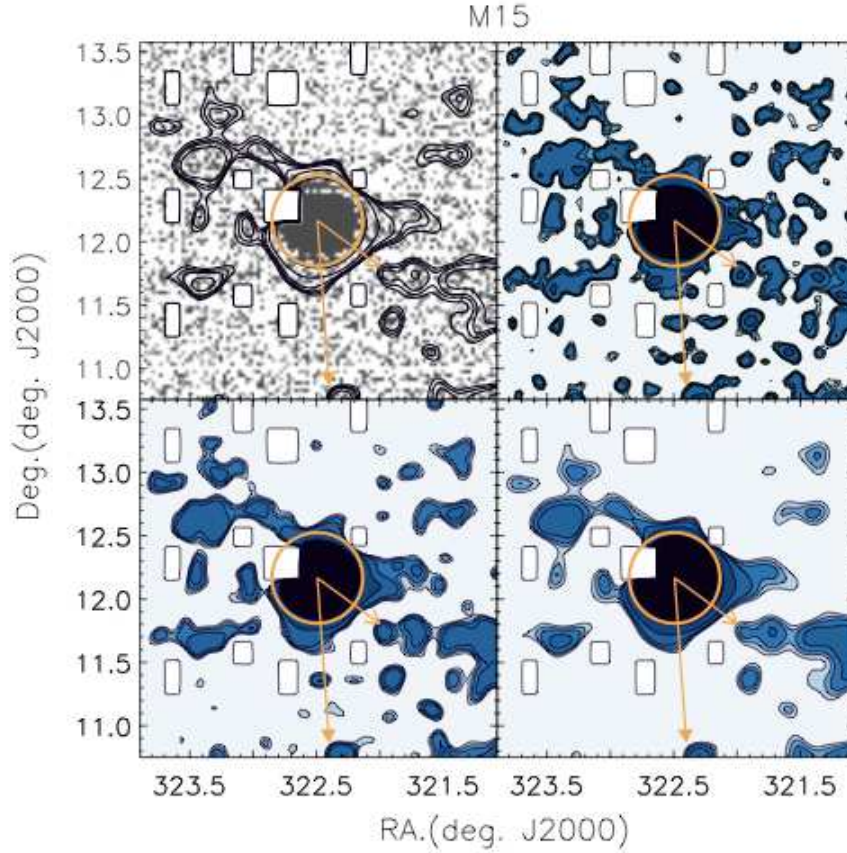


Fig. 5.— From top-left to bottom-right, the raw star count map around M15 and the surface density maps smoothed by Gaussian kernel values of 0.090° , 0.135° , and 0.195° , overlaid with isodensity contour levels of 2σ , 2.5σ , 3σ , 4σ , 8σ , and 30σ above the background level. The circle indicates a tidal radius of M15. The short and long arrows represent the direction of the Galactic center and of the cluster’s proper motion, respectively.

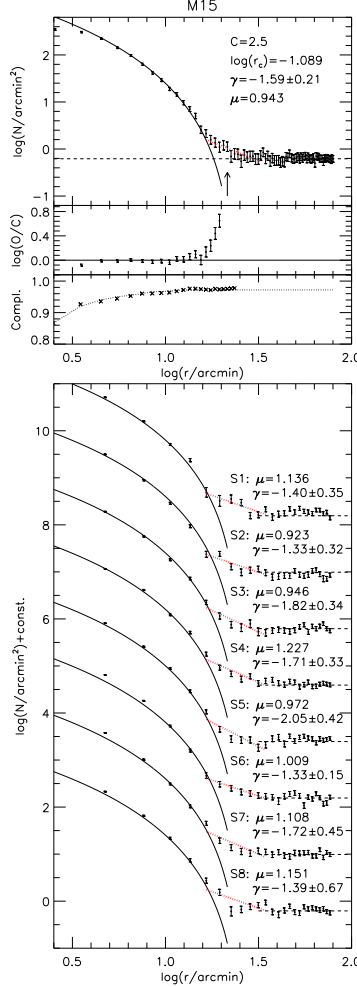


Fig. 6.— *Upper* : Radial surface density profile of M15 with a theoretical King model of $c = 2.5$ (solid curve). Residuals, $\log(O/C)$, after subtracting the values predicted by the King model from the observed surface densities are also plotted. Radial completeness, the ratio of the number of recovered artificial stars and the total number of stars, and its trend (dotted line) are added. The profile within the detected overdensity region, $\sim 0.7r_t \leq r \leq \sim 1.5r_t$, is represented by a power-law, i.e., a dotted straight line in logarithmic scale with a slope of $\gamma = -1.59 \pm 0.21$. The mean number density of stars in the overdensity region is estimated as $\mu = 0.943$ per arcminute square. The dashed horizontal line indicates the background density level, and an arrow represents the tidal radius of M15. *Lower* : Radial surface density profiles of eight different angular sections (S1~S8). For clarity, the surface densities from S1 to S8 are given zero-point offsets with values of $\text{const.} = 8.4, 7.2, 6.0, 4.8, 3.6, 2.4, 1.2, 0.0$. Dotted lines indicate the power-law fit to the overdensity region of $\sim 0.7r_t \leq r \leq \sim 1.5r_t$ with γ as a slope. μ is the mean density in the overdensity region.

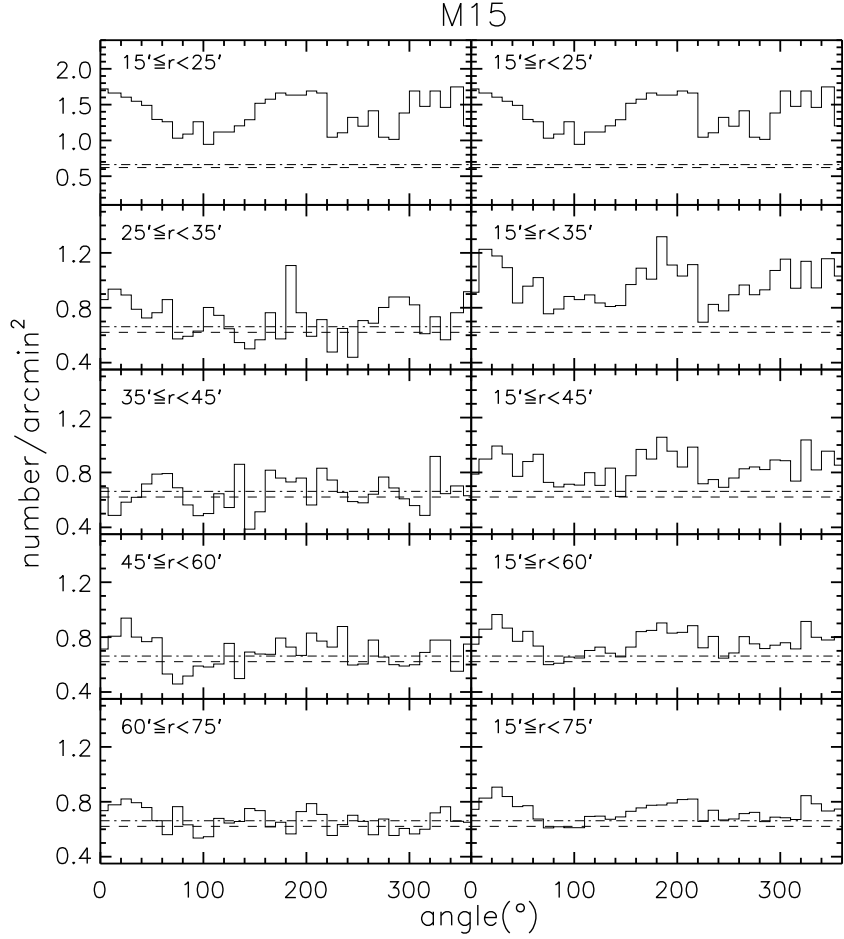


Fig. 7.— The annular (left panels) and radially cumulative (right panels) azimuthal number density profiles of M15 with an angular bin size of 10° . The radial bins are set to be $10'$ for the inner three annuli and $15'$ for the outer two annuli. The horizontal dashed lines are the determined background density level and dashed dotted lines are the level of 1σ deviation above background level.

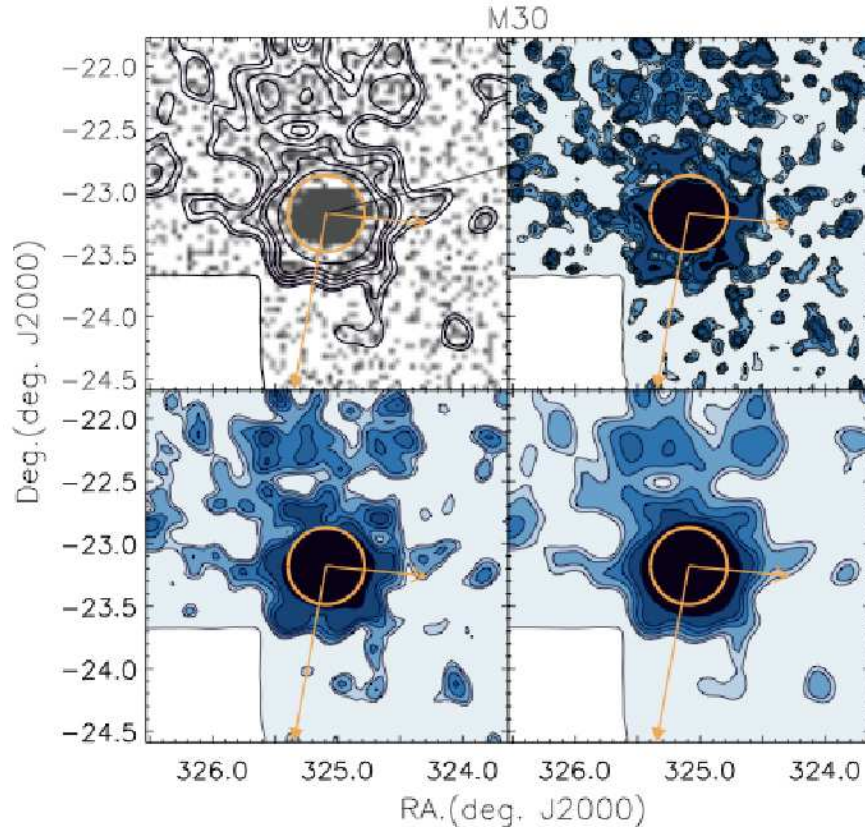


Fig. 8.— The raw star count map around M30 and the surface density contour maps smoothed by Gaussian kernel values of 0.084° , 0.147° , and 0.210° . The contour levels are the background level, 0.5σ , 1.5σ , 2.5σ , 3.5σ , and 8σ above the background level. The circle indicates a tidal radius of M30. The short and long arrows represent the direction of the Galactic center and of the cluster’s proper motion, respectively.

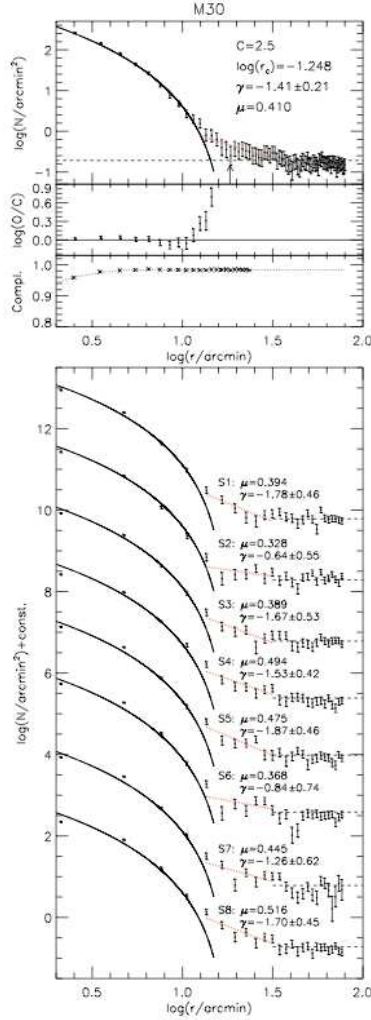


Fig. 9.— *Upper* : Radial surface density profile of M30 with a theoretical King model of $c = 2.5$ (solid curve), residuals after subtracting the values predicted by the King model, and radial completeness and its trend (dotted line). The profile within the detected overdensity region, $\sim 0.7r_t \leq r \leq \sim 2r_t$, is represented by a power-law, i.e., a dotted straight line in logarithmic scale with a slope of $\gamma = -1.41 \pm 0.21$. The mean number density of stars in the overdensity region is estimated as $\mu = 0.410$ per arcminute square. The dashed horizontal line indicates the background density level, and an arrow represents the tidal radius of M30. *Lower* : Radial surface density profiles to eight different angular sections (S1~S8). For clarity, the surface densities from S1 to S8 are given zero-point offsets with values of const.= 10.5, 9.0, 7.5, 6.1, 4.7, 3.3, 1.5, 0.0. Dotted lines indicate the power-law fit to the overdensity region with γ as a slope. μ is the mean density in the overdensity region.

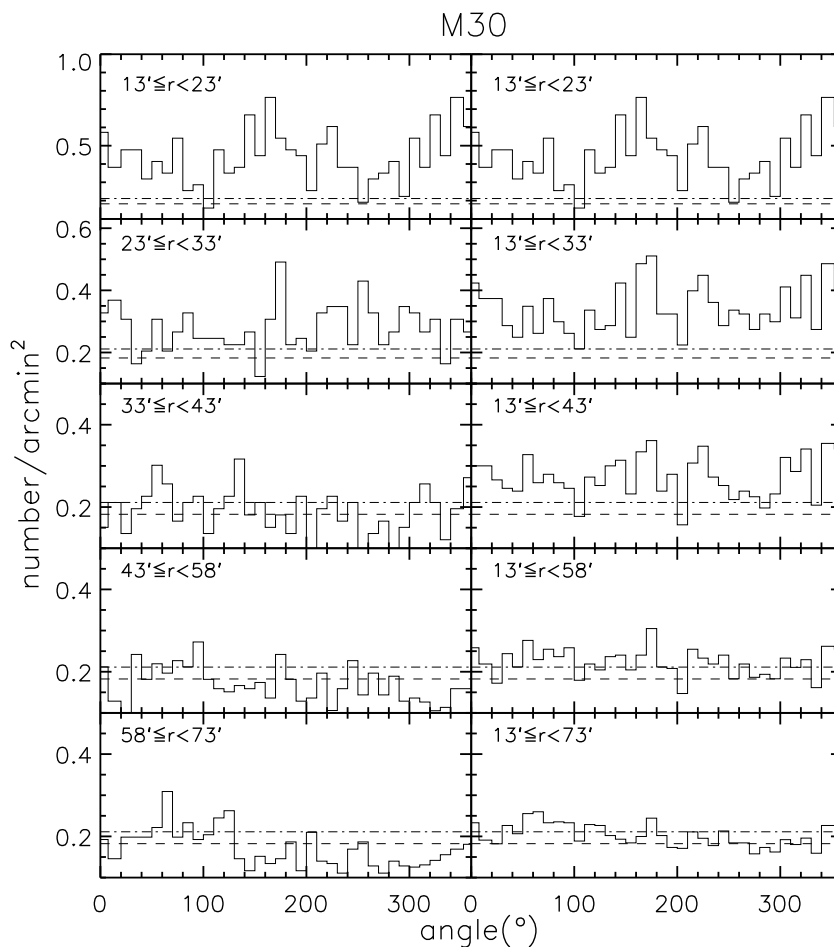


Fig. 10.— The annular (left panels) and radially cumulative (right panels) azimuthal number density profiles of M30 with an angular bin size of 10° . The radial bins are set to be $10'$ for the inner three annuli and $15'$ for the outer two annuli. The horizontal dashed lines are the determined background density level and dashed dotted lines are the level of 1σ deviation above background level.

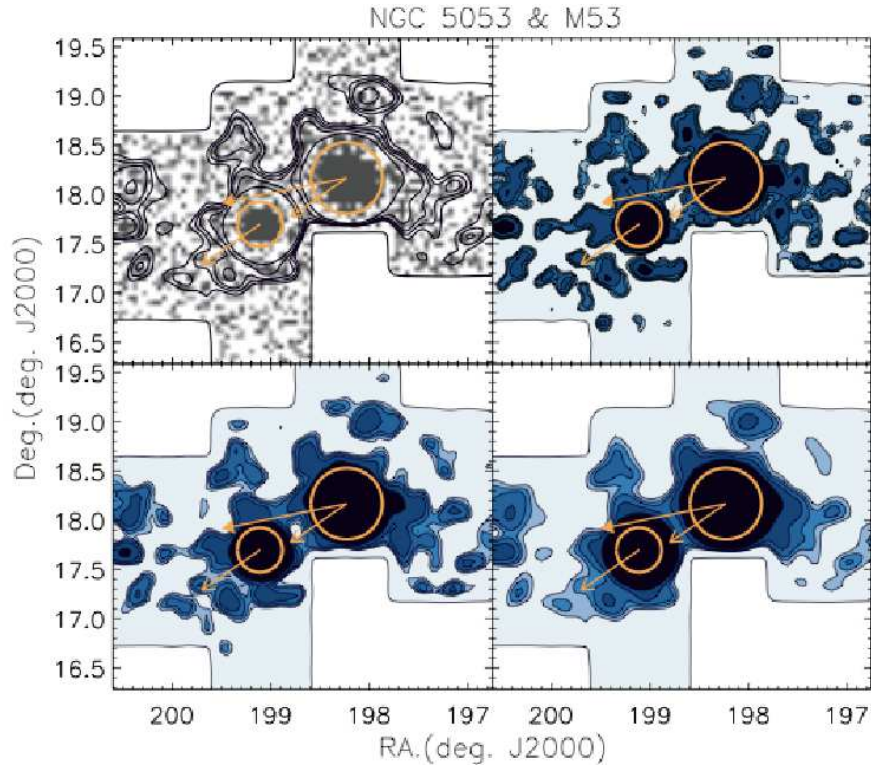


Fig. 11.— The raw star count map around M53 and NGC 5053 and the surface density contour maps smoothed by Gaussian kernel values of 0.125° , 0.175° , and 0.240° . The contour levels are the background level, 2σ , 4σ , 8σ , and 20σ above the background level. The circles indicate tidal radii of M53 and NGC 5053. The long arrow from M53 indicates the direction of the cluster’s proper motion. The short arrows represent the direction of the Galactic center.

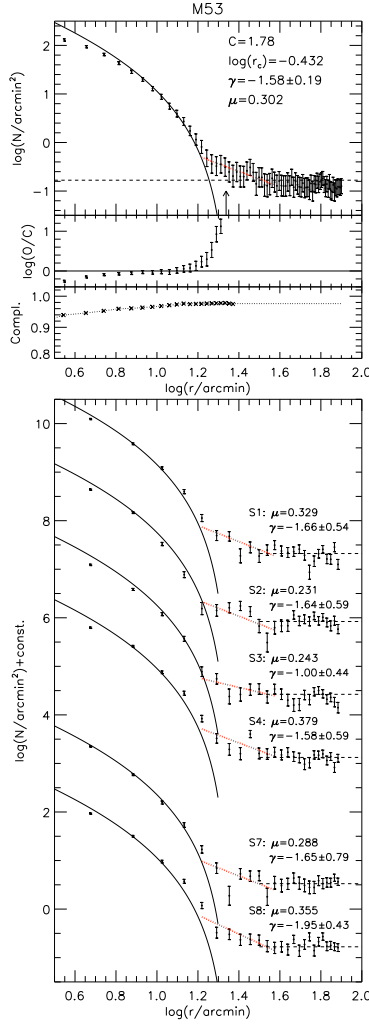


Fig. 12.— *Upper* : Radial surface density profile of M53 with a theoretical King model of $c = 1.78$ (solid curve), residuals after subtracting the values predicted by the King model, and radial completeness and its trend (dotted line). The profile within the detected overdensity region, $\sim 0.7r_t \leq r \leq \sim 1.6r_t$, is represented by a power-law, i.e., a dotted straight line in logarithmic scale with a slope of $\gamma = -1.58 \pm 0.19$. The mean number density of stars in the overdensity region is estimated as $\mu = 0.302$ per arcminute square. The dashed horizontal line indicates the background density level, and an arrow represents the tidal radius of M53. *Lower* : Radial surface density profiles of six different angular sections. For clarity, the surface densities from S1, S2, S3, S4, S7 and S8 are given zero-point offsets with values of $\text{const.} = 8.1, 6.7, 5.2, 3.9, 1.3, 0.0$. Dotted lines indicate the power-law fit to the overdensity region with γ as a slope. μ is the mean density in the overdensity region.

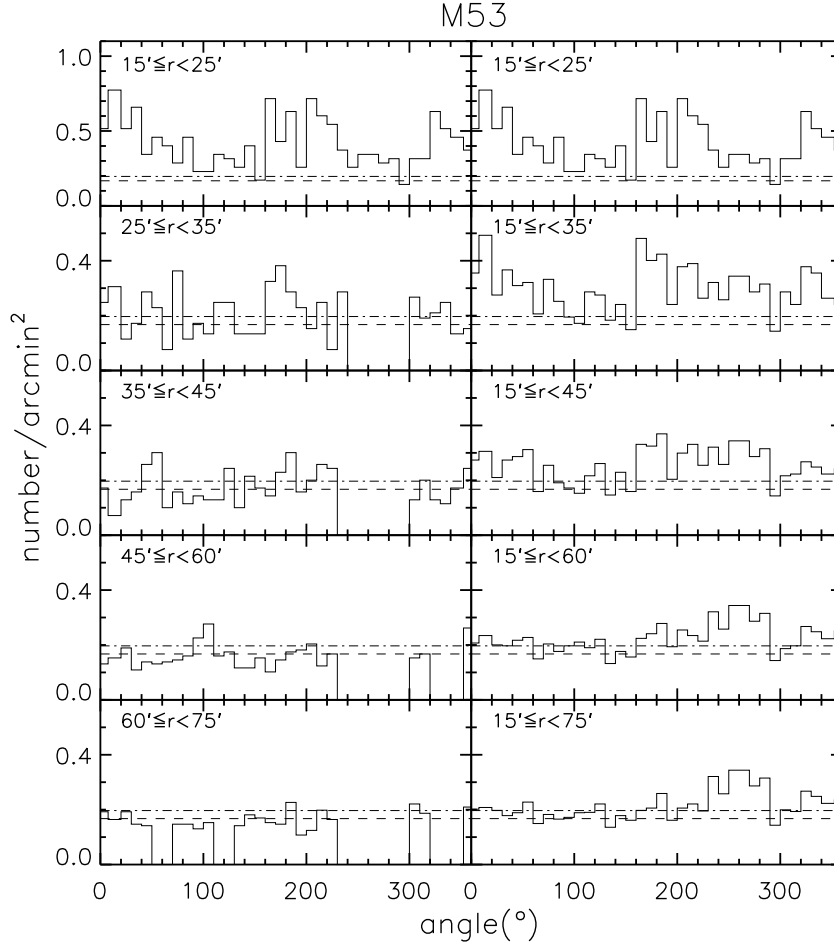


Fig. 13.— The annular (left panels) and radially cumulative (right panels) azimuthal number density profiles of M53 with an angular bin size of 10° . The radial bins are set to be $10'$ for the inner three annuli and $15'$ for the outer two annuli. The blank bins correspond to the areas without photometric data and the area within the tidal radius of the neighbor cluster NGC 5053. The horizontal dashed lines are the determined background density level and dashed dotted lines are the level of 1σ deviation above background level.

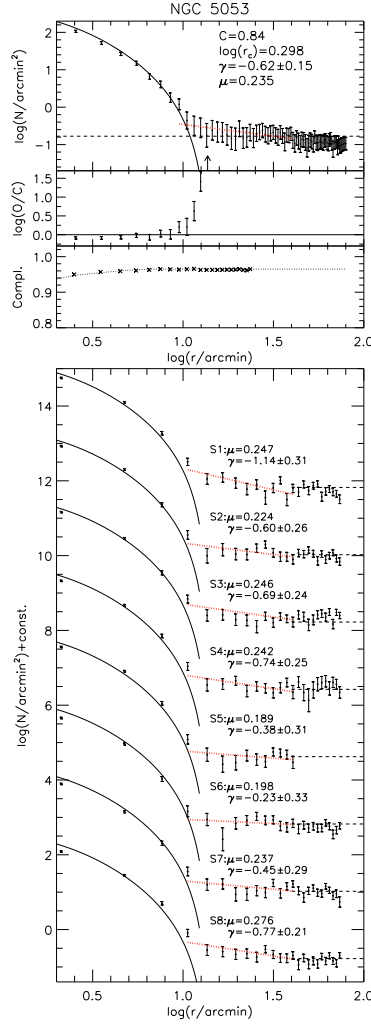


Fig. 14.— *Upper* : Radial surface density profile of NGC 5053 with a theoretical King model of $c = 0.84$ (solid curve), residuals after subtracting the values predicted by the King model, and radial completeness and its trend (dotted line). The profile within the detected overdensity region, $\sim 0.7r_t \leq r \leq \sim 2.5r_t$, is represented by a power-law, i.e., a dotted straight line in logarithmic scale with a slope of $\gamma = -0.62 \pm 0.15$. The mean number density of stars in the overdensity region is estimated as $\mu = 0.235$ per arcminute square. The dashed horizontal line indicates the background density level, and an arrow represents the tidal radius of NGC 5053. *Lower* : Radial surface density profiles of eight different angular sections (S1~S8). For clarity, the surface densities from S1 to S8 are given zero-point offsets with values of $\text{const.} = 12.6, 10.8, 9.0, 7.2, 5.4, 3.6, 1.8, 0.0$. Dotted lines indicate the power-law fit to the overdensity region with γ as a slope. μ is the mean density in the overdensity region.

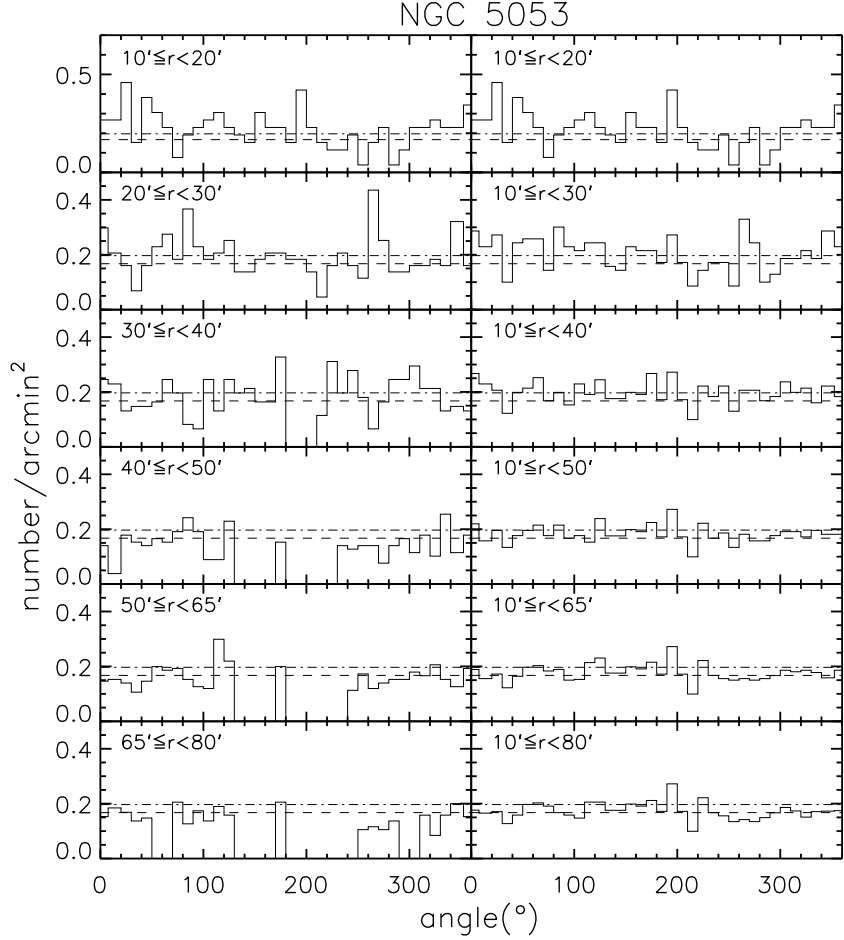


Fig. 15.— The annular (left panels) and radially cumulative (right panels) azimuthal number density profiles of NGC 5053 with an angular bin size of 10° . The radial bins are set to be $10'$ for the inner four annuli and $15'$ for the outer two annuli. The blank bins correspond to the areas without photometric data and the area within the tidal radius of the neighbor cluster M53. The horizontal dashed lines are the determined background density level and dashed dotted lines are the level of 1σ deviation above background level.

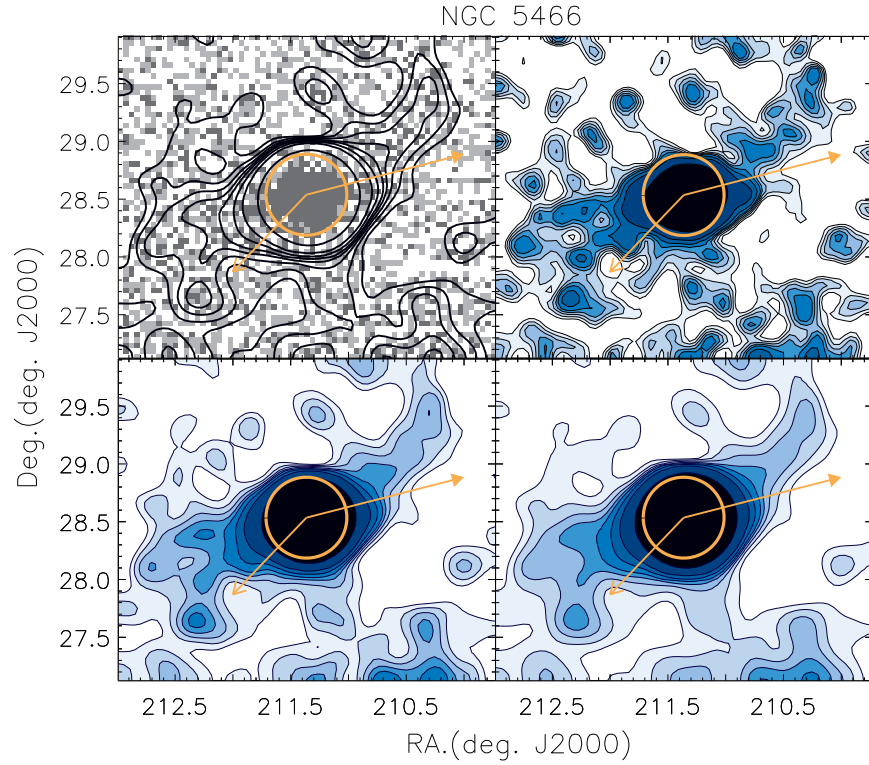


Fig. 16.— The raw star count map around NGC 5466 and the surface density contour maps smoothed by Gaussian kernel values of 0.168° , 0.264° , and 0.312° . The contour levels are the background level, 1σ , 2σ , 3σ , 4σ , 6σ , 10σ , and 40σ above the background level. The circle indicates a tidal radius of NGC 5466 (Lehmann & Scholz 1997). The short and long arrows represent the direction of the Galactic center and the cluster’s proper motion, respectively.

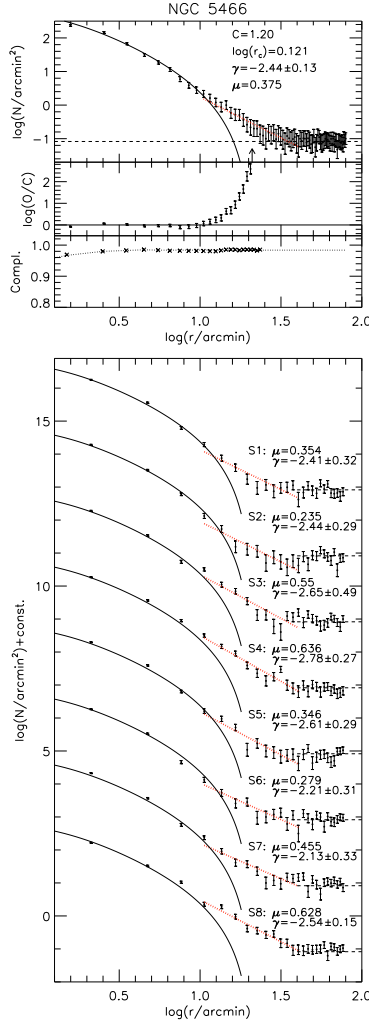


Fig. 17.— *Upper* : Radial surface density profile of NGC 5466 with a theoretical King model of $c = 1.20$ (solid curve), residuals after subtracting the values predicted by the King model, and radial completeness and its trend (dotted line). The profile within the detected overdensity region, $\sim 0.5r_t \leq r \leq \sim 2r_t$, is represented by a power-law, i.e., a dotted straight line in logarithmic scale with a slope of $\gamma = -2.44 \pm 0.13$. The mean number density of stars in the overdensity region is estimated as $\mu = 0.375$ per arcminute square. The dashed horizontal line indicates the background density level, and an arrow represents the tidal radius of NGC 5466. *Lower* : Radial surface density profiles of eight different angular sections (S1~S8). For clarity, the surface densities from S1 to S8 are given zero-point offsets with values of const.= 14.0, 12.0, 10.0, 8.0, 6.0, 4.0, 2.0, 0.0. Dotted lines indicate the power-law fit to the overdensity region with γ as a slope. μ is the mean density in the overdensity region.

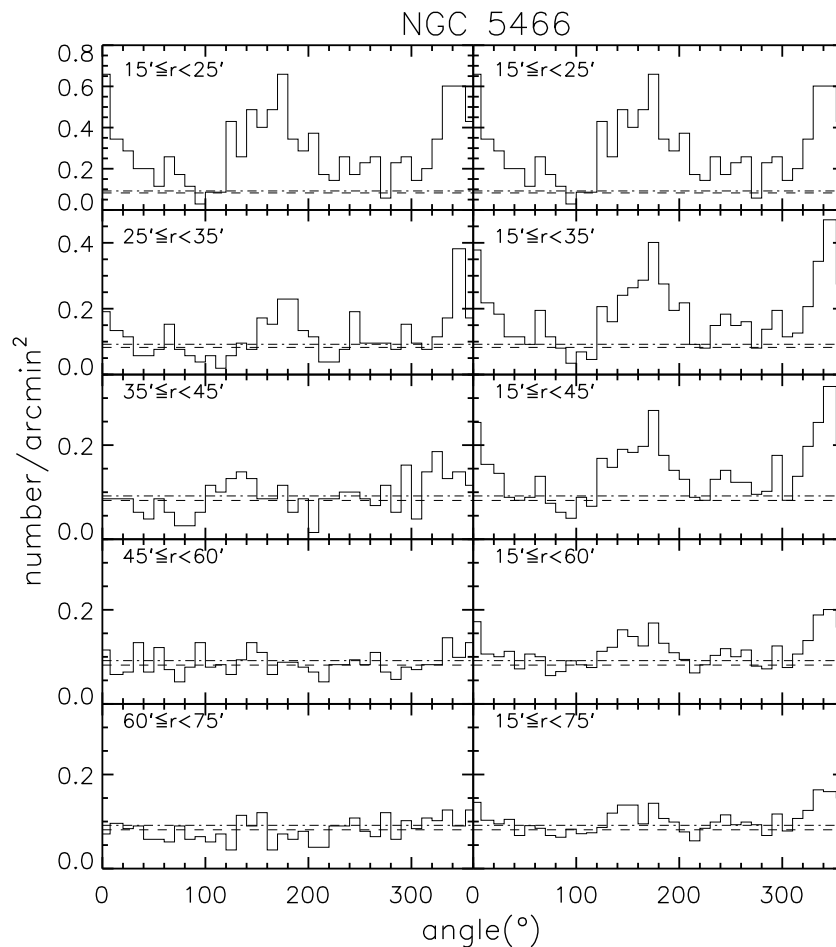


Fig. 18.— The annular (left panels) and radially cumulative (right panels) azimuthal number density profiles of NGC 5466 with an angular bin size of 10° . The radial bins are set to be $10'$ for the inner three annuli and $15'$ for the outer two annuli. The horizontal dashed lines are the determined background density level and dashed dotted lines are the 1σ deviation above background level.

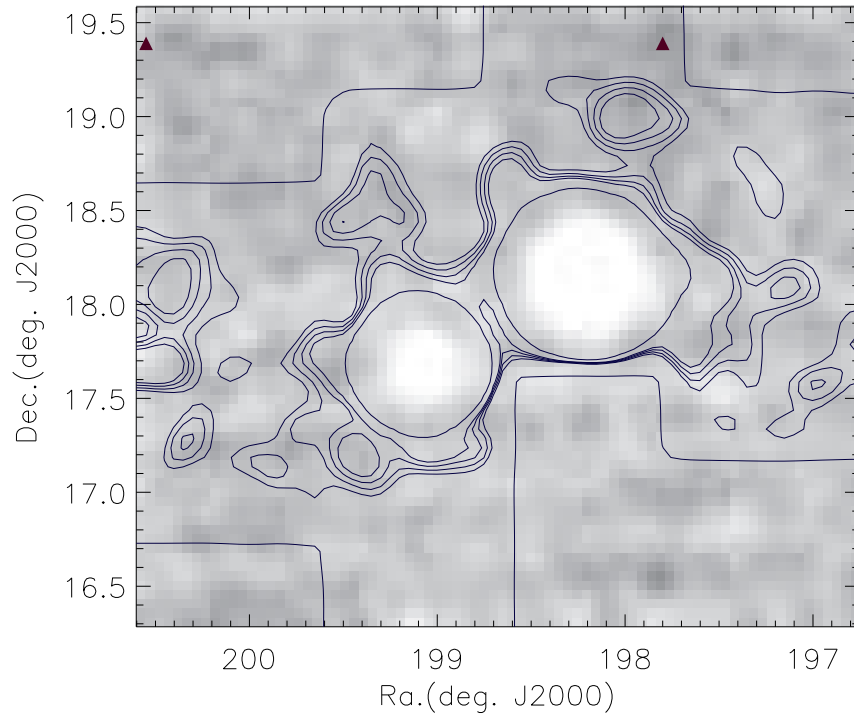


Fig. 19.— The gray scale map for the surface number density of background galaxies around M53 and NGC 5053. Background galaxies were selected by using non-pointlike SDSS sources. Filled triangles indicate Abell clusters in the observed field. The overlaid contour levels show the spatial configuration of selected stars surrounding two clusters, M53 and NGC 5053.

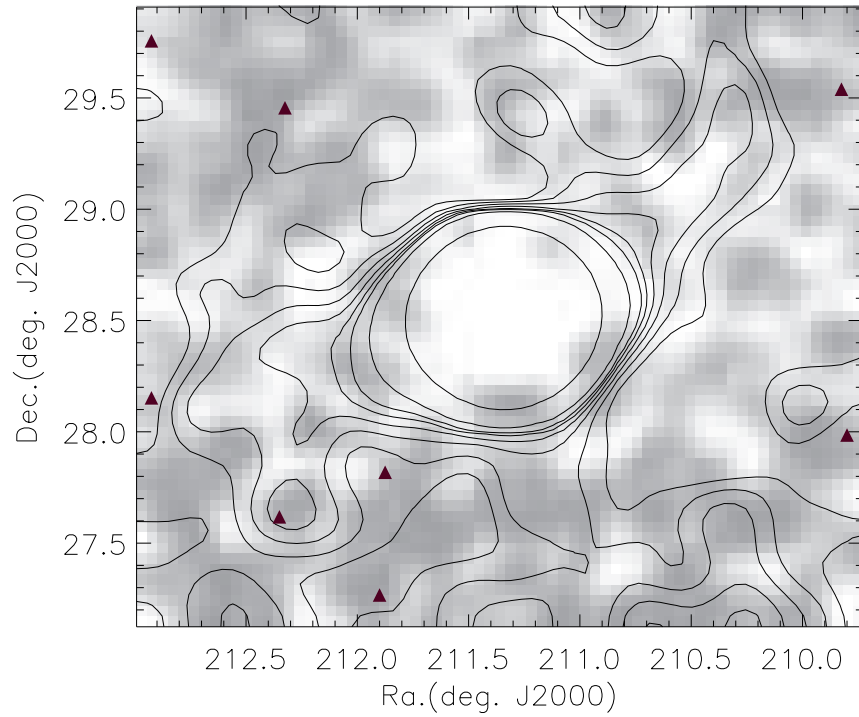


Fig. 20.— The gray scale map for the surface number density of background galaxies around NGC 5466. Background galaxies were selected by using non-pointlike SDSS sources. Filled triangles indicate eight Abell clusters in the observed field. The overlaid contour levels show the spatial configuration of selected stars surrounding NGC 5466.

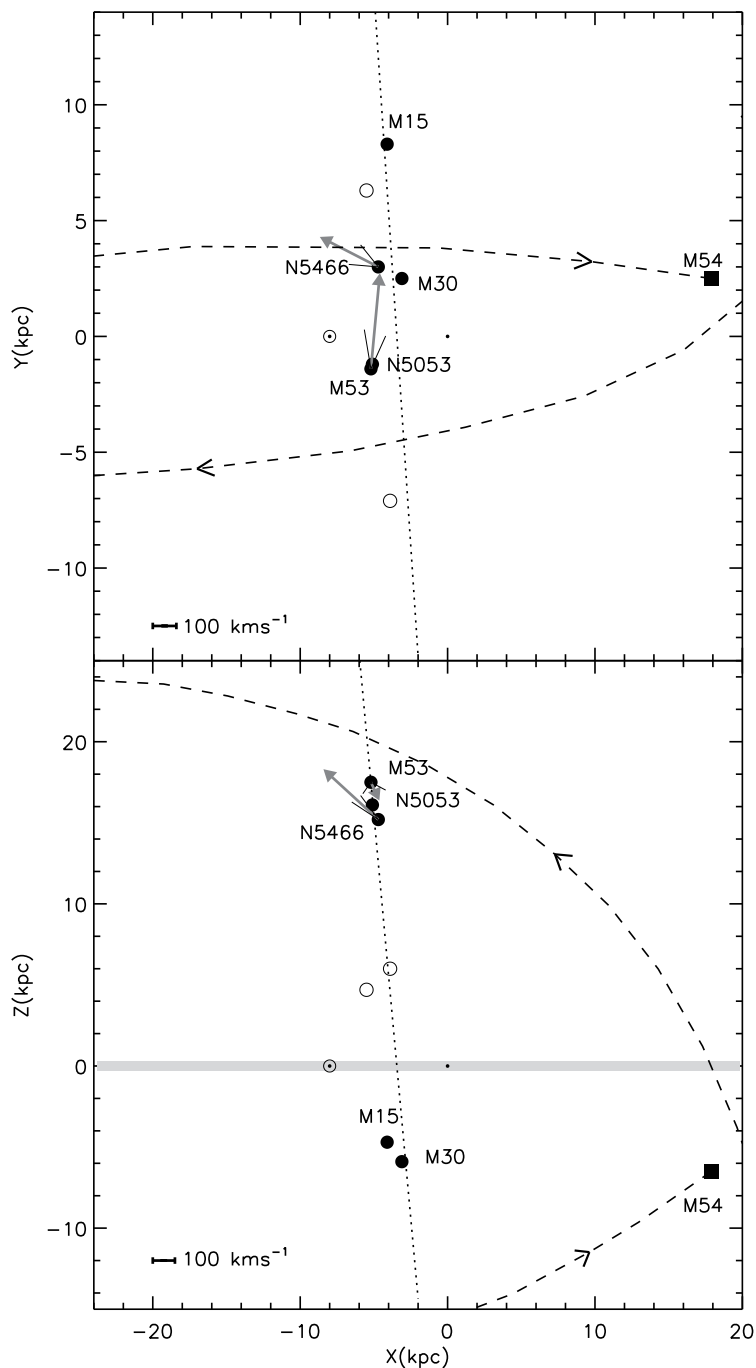


Fig. 21.— The spatial distribution of seven low-metallicity globular clusters in the Galactocentric coordinate. The Galactic plane is drawn in $X - Z$ plane, and the Sun (indicated by the circle with a dot) is at $(-8, 0, 0)$ kpc. The filled circles are five target clusters in this study, while two open circles represent M68 and M92. Space motion vectors of M53 and NGC 5466 are indicated by thick arrows with the uncertainties. The filled square marks the Sagittarius globular cluster M54. The dotted line is the Magellanic plane (Yoon & Lee 2002), and the dashed line is the Sgr orbit (Ibata & Lewis 1998) since the present time to ≈ 1 Gyr ago.

Table 1. Basic data for five target globular clusters

Target	α (J2000)	δ (J2000)	l (deg)	b (deg)	R_{sun} (kpc)	R_{GC} (kpc)	r_c (')	r_t (')	[Fe/H]
M15	21:29:58.3	12:10:01	65.01	-27.31	10.3	10.4	0.07	21.5	-2.26
M30	21:40:22.0	-23:10:45	27.18	-46.83	8.0	7.1	0.06	18.34	-2.12
M53	13:12:55.3	18:10:09	332.96	79.76	17.8	18.3	0.36	21.75	-1.99
NGC 5053	13:16:27.0	17:41:53	335.69	78.94	16.4	16.9	1.98	13.67	-2.29
NGC 5466	14:05:27.3	28:32:04	42.15	73.59	15.9	16.2	1.20	20.98	-2.22

Note. — R_{sun} and R_{GC} represent distances from the Sun and the Galactic center, respectively. r_c and r_t are the core radius and tidal radius of a cluster. Data are from Harris (1996) except for core radius and tidal radius of NGC 5466, which are from Lehmann & Scholz (1997).

Table 2. Journal of Observations

Target	Filter	Exp.Time (s)	FWHM (")	Number of fields
M15	g'	135	0.8	9
	r'	170	0.8	9
	i'	260	0.8	9
M30	g'	110	0.7	8
	r'	125	0.7	8
	i'	160	0.6	8
M53 / NGC 5053	g'	90	1.0	9
	r'	180	1.0	9
	i'	480	0.9	9
NGC 5466	g'	90	0.9	9
	r'	180	0.8	9
	i'	480	0.7	9

Table 3. The coefficients a and b for a rotational transformation of the $(g' - r', r' - i')$ plane to (c_1, c_2) plane, for each cluster.

Target	a	b
M15	0.905	0.425
M30	0.909	0.417
M53 / NGC 5053	0.909	0.416
NGC 5466	0.912	0.411